Coherent Vibrations of Adsorbates Induced by Femtosecond Laser Excitation

Yoshiyasu Matsumoto* and Kazuya Watanabe

National Institutes of Natural Sciences, Institute for Molecular Science, Okazaki, Aichi 444-8585, Japan, and Department of Photoscience, School of Advanced Sciences, The Graduate University for Advanced Studies (Sokendai), Hayama, Kanagawa 240-0193, Japan

Received January 30, 2006 (Revised Manuscript Received July 14, 2006)

Contents

* Corresponding author. E-mail: matsumoto@ims.ac.jp.

1. Introduction

Surface reactions take place under the influence of nuclear motions associated with intra-adsorbate and adsorbate−substrate vibrational modes. Thus, vibrational excitation and decay at a surface are of great interest in surface chemistry and heterogeneous catalysis.[1,2] Central issues of surface chemistry include which vibrational mode is most relevant to a reaction, how vibrational energy is transferred to a specific bond of an adsorbate to surmount the activation barrier of the reaction, and how surface phonons are involved in the reaction. These questions all relate to vibrational relaxation at surfaces, which is very sensitive to the adsorbate−substrate and inter-adsorbate interactions. Therefore, for a clear understanding of surface chemistry, it is vital to accumulate a wide range of information about vibrational relaxation.

Vibrational relaxation at surfaces has been extensively studied experimentally and theoretically, and excellent reviews[3−7] on this subject have been published. Vibrational relaxation processes include population decay and pure dephasing of vibrational modes. For chemisorbed adsorbates interacting strongly with substrates, population decay was initially considered to be the most efficient process. However, it has been recognized that pure dephasing also contributes significantly to vibrational relaxation at surfaces. Hence, vibrational coherence has attracted considerable attention, and studies have been done on coherent excitation and dephasing of vibrational modes at surfaces by ultrafast laser spectroscopy.

Studies of loss of vibrational coherence on surfaces were performed even before ultrafast laser sources were intro-

10.1021/cr050165w CCC: $59.00
Published on Web 09/20/2006

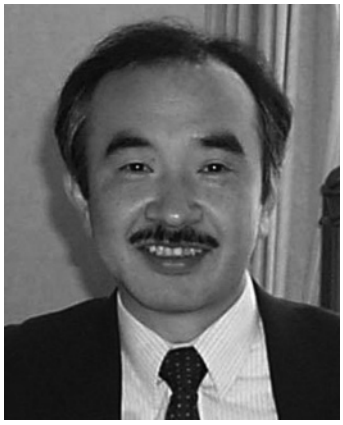

Yoshiyasu Matsumoto was born and raised in Kyoto, Japan. He received his Bachelor and Master degrees in industrial chemistry from Kyoto University and Ph.D. in reaction chemistry from the University of Tokyo in 1981. Following appointments as a postdoctoral researcher in the University of Pittsburgh working with Professor David W. Pratt and as a research scientist at RIKEN institute working with Dr. M. Takami, he was appointed as Associate Professor at Institute for Molecular Science (IMS) in 1990. He moved to the Graduate University for Advanced Studies (SOKENDAI) as a Full Professor in 1997, and has been a Professor at IMS since 2004 with a joint appointment in SOKENDAI. He received the Award for Creative Work from the Chemical Society of Japan in 2006. His current research interests include photoinduced dynamics and reactions at surfaces and interfaces, catalytic reactions, and the electronic structure and reactivity of nano-structured materials.

Kazuya Watanabe is a research associate at the Institute for Molecular Science in Japan. He was born in 1970 in Nara, Japan. In 1997, he received his Ph.D. in applied physics from Osaka University after completing his thesis work on ultrafast electronic dynamics in organic solids under the direction of Prof. H. Masuhara. Then he moved to the Institute for Molecular Science to join the research group of Prof. Yoshiyasu Matsumoto. Since then, he has worked on ultrafast electronic and vibrational dynamics at surfaces by using femtosecond pump–probe spectroscopy. His current research interests include ultrafast dynamics of surface adsorbates and laser control of surface dynamics.

duced. Even in thermal equilibrium, the line shape of an absorption band of an adsorbate vibration mode contains information on pure dephasing. Spectral line width analysis is a major source of information on loss of coherence. However, spectral line widths are often broadened inhomogeneously. Thus, it may be complicated to identify the various contributions to the line widths by frequency-domain spectroscopy. Consequently, in addition to frequency-domain measurements, time-domain measurements with picosecond laser pulses have been conducted to populate the vibrationally excited states of adsorbates and to probe the decay process,[5,6] providing a direct means to measure population decay times.

Recent developments in femtosecond-laser-pulse generation techniques have further advanced the understanding of coherent motions of adsorbates and their relaxation dynamics. Laser pulses with durations sufficiently shorter than the vibrational period of an adsorbate vibrational mode make it possible to create coherent nuclear wave packets on excited[8] and ground potential energy surfaces.[9] Various time-resolved nonlinear spectroscopy methods such as second harmonic generation (SHG), sum frequency generation (SFG), and two-photon photoemission (2PPE) have been used to study the evolution and dephasing of nuclear wave packets at surfaces.

Moreover, the advent of femtosecond-laser technology provides exciting opportunities to probe chemical reactions in real time and even to control the reactions.[10,11] For example, tailored light pulses optimized with a genetic algorithm have been successfully employed to control chemical reactions in gas and liquid phases.[12] Although we are still in the very early stages of coherent control in surface chemistry, attempts have been recently made to control nuclear motions at surfaces by tailored femtosecond-laser pulses.[8,13,14] The major obstacle for this type of reaction control is the various incoherent perturbations from the heat bath that adsorbates interact with, since these incoherent perturbations cause rapid dephasing. Therefore, to realize reaction control at surfaces it is vital to know how coherence is lost by those perturbations and to clarify the most effective cause of energy and phase relaxation.

In this review, we describe recent progress in excitation and dephasing of coherent motions at surfaces and interfaces by irradiation with femtosecond-laser pulses. We concentrate on studies on time-resolved nonlinear spectroscopy, which is a major source of information on coherent vibrations at surfaces. Time-resolved X-ray diffraction is also a very powerful method, but it has only been applied to coherent motions in nanostructured materials and bulk crystals.[15,16]

The review is organized as follows. In the next section (Section 2) the basics of coherent excitation and dephasing are presented, to explain the concepts of coherence and dephasing. We then consider possible mechanisms for coherent excitation at surfaces in Section 3 and time-resolved nonlinear spectroscopy to monitor the evolution of coherent motions in Section 4. In Section 5, we focus on the vibrational relaxation of CO on metal surfaces, since CO is a prototype adsorbate and has been most extensively studied. In Section 6, we describe the applications of femtosecond-time-resolved SHG to coherent phonons at semiconductor surfaces and interfaces. In Section 7, we describe coherent motions and their dynamics on metal surfaces covered with alkali-metal atoms. We extend the subject further to studies of coherent phonons at the surfaces of ferromagnetic ultrathin metal films in Section 8, where coherent phonons couple to magnons. Then, we describe attempts to control coherent motions of alkali atoms on metal surfaces in Section 9. Note that the coverage of adsorbate represented by "ML" in this review is defined as the coverage referenced to the metal substrate in atom number density, unless otherwise noted.

2. Coherence and Dephasing

In this section, we describe the fundamental concepts of coherence and dephasing of a quantum system using the standard formulation of density matrix theory.[17] We first introduce the phenomenological relaxation terms due to incoherent interactions of the quantum system with the heat bath. We then present the equation of motion of the

amplitude of a quantum oscillator, which plays a central role in describing coherent vibrations and phonons in subsequent sections of this review. Finally, we show that pump−probe time-domain measurements provide an extra observable that cannot be obtained from steady-state frequency-domain measurements, i.e., the initial phase of a coherent oscillator.

2.1. Coherent Vibrations and Phonons

We begin by defining wave packets. Let $\phi_n(r)$ be the eigenstates of the time-independent Schrödinger equation

$$H_0\phi_n(r) = \epsilon_n\phi_n(r) \tag{1}$$

where H_0 is the Hamiltonian and ϵ_n is the nth eigenenergy. When a system is prepared in a superposition of eigenstates at $t = t_0$, i.e.,

$$\psi(r, t) = \sum_n c_n(t_0)\phi_n(r)e^{-i\epsilon_n(t-t_0)/\hbar} \tag{2}$$

the system is nonstationary and evolves in time according to the time-dependent Schrödinger equation

$$i\hbar\frac{\partial}{\partial t}\psi(r, t) = H_0\psi(r, t) \tag{3}$$

The wave function represented by eq 2 is called a wave packet.[18] For example, for an isolated molecule whose vibrational motion is represented by a harmonic oscillator, the wave packet composed of the vibrational eigenstates ϕ_0 and ϕ_1 oscillates back and forth with an eigenfrequency ω_0. In the case of extended systems such as phonons in bulk solids and at surfaces, the nonstationary state described by a superposition of wave functions with different momenta k in the range from $k_0 - \delta k$ to $k_0 + \delta k$

$$\psi(r, t) = \frac{1}{2\pi^{3/2}}\int_{k_0-\delta\kappa}^{k_0+\delta\kappa} g(k)e^{ik\cdot r-\omega(k)t}d^3k \tag{4}$$

becomes a wave packet spatially localized with a width of $\sim 1/\delta k$.

Although the description of a quantum system using wave functions makes it intuitively easy to visualize the coherent motion of the system, in practice we need to deal with a statistical mixture of states. For this purpose, the formalism using the density operator ρ is more suitable. In this formalism, the diagonal matrix elements of the density operator ρ_{nn} represent the population of the nth state, while the off-diagonal matrix elements $\rho_{nm}(n \neq m)$ represent coherence in the ensemble. The off-diagonal elements are the counterparts to the linear superposition in the wave function description and express interference between the nth and mth states. Thus, the off-diagonal elements ρ_{nm} take nonzero values only if the two states have a definite phase relationship.

The time evolution of the density operator is described by

$$i\hbar\frac{\partial}{\partial t}\rho(t) = [H(t),\rho(t)] \tag{5}$$

In general, the Hamiltonian contains the interactions of an ensemble of quantum systems with its environment, i.e., the heat bath. These interactions cause random fluctuations and contribute to energy dissipation processes. Phenomenological relaxation terms are added to eq 5 to account for such effects:[17,19]

$$\frac{\partial\rho_{nm}}{\partial t} = \frac{1}{i\hbar}[H,\rho]_{nm} - \gamma_{\mathrm{nm}}\rho_{\mathrm{nm}}, (n \neq m) \tag{6}$$

$$\frac{\partial\rho_{nn}}{\partial t} = \frac{1}{i\hbar}[H,\rho]_{nn} + \sum_{\epsilon_m>\epsilon_n}\Gamma_{nm}\rho_{mm} - \sum_{\epsilon_m<\epsilon_n}\Gamma_{mn}\rho_{nn} \tag{7}$$

where the relaxation terms γ_{nm} represent the dephasing rate of ρ_{nm} and includes contributions from the total population decay rates Γ_j out of level j, i.e., $\Gamma_j = \sum_{j'(\epsilon j'<\epsilon j)}\Gamma_{j'j}$, and the pure dephasing rate γ^*_{nm}:

$$\gamma_{nm} = \frac{1}{2}(\Gamma_n + \Gamma_m) + \gamma^*_{nm} \tag{8}$$

In the two level approximation, the population decay rate of the ground state Γ_n is zero and Γ_m and γ^*_{nm} are replaced by $1/T_1$ and $1/T_2^*$, respectively. Thus, the dephasing time $T_2 = 1/\gamma_{\mathrm{nm}}$ is determined by the population decay T_1 and the pure dephasing T_2^*:

$$\frac{1}{T_2} = \frac{1}{2T_1} + \frac{1}{T_2^*} \tag{9}$$

Dephasing represents a loss of coherence, i.e., a loss of initial phase memory. Quantum mechanically, this implies that the phase relationship between the nth and mth states is lost, i.e., $\rho_{nm} \rightarrow 0$ $(n \neq m)$, with a characteristic decay time constant of T_2.

We briefly note the processes that contribute to the vibrational relaxation of adsorbates on metal and semiconductor surfaces. For population decay, vibrational energy must flow into other available degrees of freedoms. Thus, population decay is associated with inelastic collisions with substrate phonons or energy dissipation due to electron−hole pair excitation in the substrate. The relative contributions of the two pathways depend on the vibrational mode of the adsorbate and the electronic structure of the substrate on which a molecule is adsorbed. On insulator and semiconductor surfaces, electron−hole pair excitation is not effective because of the band gap, and hence energy dissipation via multiphonon generation dominates. In contrast, on metal surfaces electron−hole pair excitation is an important pathway for energy dissipation.[20]

Pure dephasing is caused by fluctuations in the phase of an oscillator. Elastic collisions with bulk phonons induce abrupt changes in the phase of the oscillator, giving phase shifts. If the oscillator undergoes an impulsive elastic collision with a bulk phonon for a time interval $2\tau_c$, it propagates in an undamped manner during $2\tau_c$. However, because of the phase shifts at the beginning and end of the interval, the displacement of the oscillator before and after $2\tau_c$ is uncorrelated with the displacement during $2\tau_c$. This causes damping of the phase correlation.[21] If the vibrational mode of interest is coupled anharmonically to other low-frequency modes, this coupling induces fluctuations in the frequency of the oscillator and also contributes to pure dephasing.[3]

Information on vibrational relaxation including population decay and pure dephasing can be obtained from frequency- and time-domain spectroscopy, although it is not always

straightforward to distinguish between these two contributions. In early vibrational relaxation studies of adsorbates, it was widely believed that population decay dominates over pure dephasing. However, it was later found from the temperature dependence of absorption line widths that pure dephasing also contributes substantially to vibrational relaxation.[22] We describe these points more specifically for CO adsorbates on metal surfaces in Section 5.

2.2. Phenomenological Treatment

The expectation value of coherent vibrational displacement can be calculated by

$$\langle Q(t)\rangle = \mathrm{Tr}\{Q\rho(t)\} = \sum_{nm}\rho_{nm}Q_{mn} \tag{10}$$

where Q_{mn} is the vibrational matrix element between the mth and nth vibrational states, $\langle\phi_m|Q|\phi_n\rangle$. Since Q_{mn} takes nonzero values when $m \neq n$, nonzero off-diagonal elements, i.e., coherence, between the states $|\phi_n\rangle$ and $|\phi_m\rangle$ are essential for finite expectation values of $\langle Q(t)\rangle$. Since the coherence ρ_{nm} decays with time constant T_2, coherence has to be created much faster than T_2 to be observed in the time domain. Therefore, the time duration of an impulsive force exerted on a system has to be shorter than T_2. In the case of optical excitation by a pump laser pulse, this implies that the pulse duration of the pump pulse has to be sufficiently shorter than T_2. There are various excitation mechanisms for coherent surface vibrations and phonons, discussed in Section 3.

The equation of motion for the displacement of coherent vibration Q given by eq 10, i.e., $Q = \langle Q\rangle$, can be described phenomenologically by

$$\frac{\mathrm{d}^2}{\mathrm{d}t^2}Q + \frac{2}{T_2}\frac{\mathrm{d}}{\mathrm{d}t}Q + {\omega_0}^2 Q = \frac{F(t)}{m'} \tag{11}$$

where ω_0 and m' are the frequency and reduced mass of a coherent oscillator, respectively, and $F(t)$ is the driving force for the coherent vibration. The formal solution of eq 11 can be written as

$$Q(t) = \frac{1}{\tilde{\omega}}\int_{-\infty}^{t}\mathrm{d}t' F(t') e^{-(t-t')/T_2}\sin(\tilde{\omega}(t-t')) \tag{12}$$

where $\tilde{\omega} = \sqrt{{\omega_0}^2 - 1/{T_2}^2}$. When the system is stimulated by an impulsive force, i.e., $F(t) = \delta(t)$, the system shows free-induction decay,

$$Q(t) \propto \sin(\tilde{\omega}t - \varphi)e^{-t/T_2} \tag{13}$$

where φ is the initial phase. As we describe later, traces of damped oscillations due to the displacement of coherent vibration can be observed by time-resolved SHG spectroscopy. Since a pump pulse in practice has a finite duration, the oscillating trace of the free-induction decay is convoluted with the profile of the impulsive force $F(t)$. Other contributions also frequently appear in SHG signals at a pump−probe delay $t \approx 0$, mainly caused by hot electrons in the substrate created by a pump pulse. Thus, the initial phase is practically determined by fitting the oscillating trace after the pump pulse with an underdamped oscillating function with free parameters φ and T_2.

2.3. Comparison between Time- and Frequency-Domain Measurements

In this review, we focus on time-domain measurements of coherent vibrations at surfaces and interfaces, in which a vibrational wave packet is created by a pump pulse, and the time evolution is monitored by a probe pulse as a function of pump−probe delay. We do not discuss line shape analysis in frequency-domain measurements in detail. However, it is worth noting how the information gained by these two measurements are related to each other and which observables are unique to time-domain measurements.

Here we assume for simplicity that the adsorbate system is homogeneously broadened. When the time duration of an infrared (IR) pulse or a pump pulse for Raman excitation is much longer than the dephasing time T_2, information on vibrational relaxation can be gained from analyzing the spectral line shapes $I(\omega)$ in the IR absorption or Raman scattering spectra. Vibrational spectral line profiles can be described by the Fourier transformation of a vibrational autocorrelation function $\phi_v(t) = \langle Q(t)Q(0)\rangle_{eq}$, that is,

$$I(\omega) = \int \mathrm{d}t\phi_v(t)e^{i\omega t} \tag{14}$$

where $\langle\cdots\rangle_{\mathrm{eq}}$ denotes an equilibrium ensemble average. For a homogeneously broadened system, the autocorrelation function is given by

$$\phi_v(t) = \cos(\omega_0 t)e^{-t/T_2} \tag{15}$$

which yields a Lorentzian line profile

$$I(\omega) = I_0\frac{1}{(\omega-\omega_0)^2 + (1/T_2)^2} \tag{16}$$

Hence, the line width obtained from frequency-domain measurements gives the dephasing time T_2 provided the spectral line is homogeneously broadened.[23]

Both population decay and pure dephasing contribute to the total dephasing time (eq 9). The line profile can be analyzed as a function of temperature and adsorbate coverage to separate the contributions of these relaxation pathways. An excellent review has been given by Chabal[3] on this point. However, it is usually difficult to distinguish the contributions uniquely from line profile analysis.

An advantage of time-domain spectroscopy is that it can directly determine population decay. In this method, a pump pulse of duration Δt satisfying the condition $T_2 < \Delta t < T_1$ is used to populate the $v = 1$ vibrational excited state. Then, a probe pulse monitors the population difference between $v = 0$ and $v = 1$ as a function of pump−probe delay. This technique has been widely used in picosecond time-domain spectroscopy, such as IR transient absorption[4,24] and SFG at surfaces.[25−27]

When the duration of the pump pulse is shorter than T_2, time-resolved spectroscopy methods, such as time-resolved SHG, have another advantage. In this case, vibrational modes are coherently excited by the pump pulse, as described in Section 2.2. Thus, the optical response relevant to the displacement of $\langle Q(t)\rangle$, instead of the vibrational autocorrelation function, is directly probed by time-domain spectroscopy. Therefore, as shown in eq 13 we can determine not only the dephasing time T_2 but also the initial phase φ from the oscillating signals in the time domain.

The fact that vibrations or phonons are excited with definite phases implies that they can interfere with each other. The interference between coherent vibrations is used for the

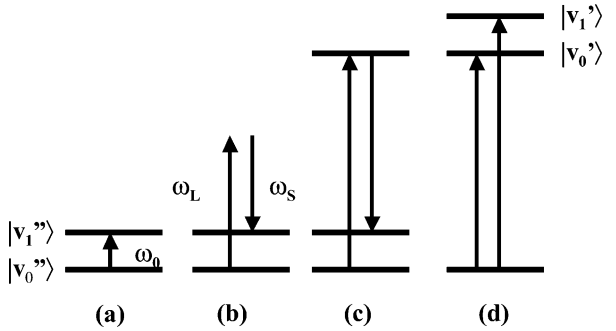

Figure 1. Excitation mechanisms for vibrational coherence: (a) IR resonant vibrational excitation, (b) nonresonant impulsive stimulated Raman excitation, and (c) and (d) are resonant impulsive stimulated Raman excitation creating vibrational coherence in the ground and electronic excited states, respectively.

selective excitation of a vibrational mode, which is discussed in Section 9.

3. Excitation Mechanisms

The excitation mechanisms for coherent bulk phonons have been extensively discussed in previous studies.[28−34] For a review, see Dekorsy et al.[35] In addition, Chang et al.[36] discussed the excitation mechanisms in detail for coherent phonons at semiconductor surfaces. In this section, we describe various excitation mechanisms for coherent vibrations of adsorbates and surface phonons based on these previous works.

3.1. Creation of Coherence by Optical Fields

The time-dependent density operator introduced in eq 5 is expanded in a perturbation approach as[37,38]

$$\rho(t) = \rho^{(0)}(t) + \rho^{(1)}(t) + \rho^{(2)}(t) + \cdots \qquad (17)$$

where $\rho^{(0)}$ is the density operator for the system at thermal equilibrium and $\rho^{(n)}$ is the nth order contribution in an electric field.

Figure 1 shows possible schemes for creation of vibrational coherence. Panel (a) represents IR resonant excitation originating from the first-order contribution. Panels (b−d) originate from the second-order contributions called impulsive stimulated Raman scattering (ISRS).[39] Panel (b) represents ISRS without electronic resonance. If the excitation pulse has a broad spectral width, stimulated Raman scattering occurs by mixing the frequency components ω_L and ω_S, fulfilling the vibrational resonant condition $\omega_L - \omega_S = \omega_0$, where ω_0 is the vibrational frequency. That is, the duration of the excitation pulse has to be less than the vibrational period to realize impulsive Raman excitation. This excitation process is substantially enhanced when the excitation wavelength is near an electronic absorption resonance, which is depicted in panel (c). In this electronic resonance case, coherent vibrational motion can be initiated also in the electronically excited state if the pump pulse duration is substantially shorter than the excited-state vibrational period, as depicted in panel (d).

The excitation schemes in panels (c) and (d) can be separately discussed only if electronic dephasing is completed.[39] Before dephasing, vibrational wave packets propagate on the ground and excited potential energy surfaces with coherent coupling between the two electronic states. In practice, since electronic dephasing times are substantially shorter than the oscillation frequencies of the vibrational modes of adsorbate and surface phonon modes on semiconductor and metal surfaces, we do not discuss the case of coherent coupling between the two electronic states in this review.

Note that off-diagonal terms of the density matrix are by definition (see Section 2.1) responsible for excitation of coherent oscillations rather than diagonal terms. These off-diagonal terms prepared by a pump pulse are the origin of a macroscopic polarization oscillating with the frequency of a coherent phonon mode. The created coherence and its dephasing are detected through the interaction between the polarization of the medium and the electromagnetic field of a probe pulse, as described in Section 4.

3.2. Infrared Resonant Vibrational Excitation

We consider now the simplest excitation scheme, Figure 1, panel (a), where an adsorbate system interacts with an IR radiation field $E(t)$ that contains a Fourier component resonant with a vibrational frequency of the adsorbate, ω_0. Under the dipole approximation, the total Hamiltonian H is written as

$$H = H_0 - \mu E(r, t) \qquad (18)$$

where H_0 is the Hamiltonian of the system in the absence of the radiation field and μ is the dipole moment operator. Thus, the effective force exerted on the adsorbate is

$$F(r, t) = e^* E(r, t) \qquad (19o)$$

where e^* is the effective dynamic charge. According to eqs 6 and 7, the density matrix equations of motion can be written under the two-level approximation as

$$\frac{d\rho_{nm}}{dt} = \left(-i\omega_0 - \frac{1}{T_2}\right)\rho_{nm} + \frac{i}{\hbar}V_{nm}(\rho_{nn} - \rho_{mm}) \qquad (20)$$

$$\frac{d\rho_{nn}}{dt} = \frac{1}{i\hbar}(V_{nm}\rho_{mn} - \rho_{nm}V_{mn}) - \frac{1}{T_1}\rho_{nn} \qquad (21)$$

$$\rho_{mm} = 1 - \rho_{nn} \qquad (22)$$

$$\rho_{nm} = \rho_{mn}^* \qquad (23)$$

Here, $V_{nm} = V_{mn}^* = \langle\phi_n| - \mu E(t)|\phi_m\rangle = -\langle\phi_n|\mu|\phi_m\rangle E(t)$ and $\langle\phi_n|\mu|\phi_m\rangle$ is the transition dipole matrix element between the vibrational states of $|\phi_n\rangle$ and $|\phi_m\rangle$.

If the system interacts with a resonant IR pulse with a width shorter than T_2, an adsorbate vibrational wave packet is created. Suppose that the IR pulse has a delta function-like profile at $t = 0$ to create the vibrational coherence $\rho_{nm}(0)$. Since the off-diagonal density matrix elements decay as

$$\rho_{nm}(t) = \rho_{nm}(0)e^{-(i\omega_0 + 1/T_2)t} \qquad (24)$$

the macroscopic polarization reveals the free-induction decay

$$P(t) = N\langle\mu\rangle = NTr(\rho\mu) = N\sum_{nm}[\rho_{nm}(0)\mu_{mn}e^{-i\omega_0 t} + \text{c.c.}]e^{-t/T_2} \qquad (25)$$

The dephasing processes can be monitored in various time-

domain spectroscopy methods including time-resolved infrared saturation spectroscopy[6] and time-resolved SFG.[7,27] Note that the off-diagonal density matrix elements can be nonzero, i.e., vibrational coherence can be created, even if the system interacts with monochromatic coherent IR radiation with a frequency in resonance with the transition frequency of a vibrational mode.

3.3. Impulsive Raman Excitation

Raman processes originating from the second-order contribution in eq 17 can create vibrational coherence at surfaces as shown in the excitation scheme, Figure 1, panel (b). Expanding the polarizability tensor α_{kl} in terms of the local vibrational coordinate Q to the first order, we obtain the relation

$$\alpha_{kl} = \alpha_{kl}^{\circ} + \left(\frac{\partial \alpha}{\partial Q}\right)_{kl} Q \tag{26}$$

The Hamiltonian of the adsorbate system is written as

$$H = H^{\circ} - \frac{1}{2} Q \sum_{k,l} \left(\frac{\partial \alpha}{\partial Q}\right)_{kl} E_k E_l \tag{27}$$

Here, E_k denotes a component of the optical field involved in the Raman process. The effective force exerted on the adsorbate by the optical fields is

$$F = \frac{1}{2} \sum_{k,l} \left(\frac{\partial \alpha}{\partial Q}\right)_{kl} E_k E_l \tag{28}$$

In combination with eq 11, this can be used to describe the evolution of the coherent vibration.

Merlin and co-workers[31,32,34] have developed a theory of impulsive stimulated Raman excitation of coherent bulk phonons. The concepts of this theory can also be applied to the excitation of coherent surface phonons. The impulsive force on a system can be represented by

$$F(t) \equiv \langle \Xi \rangle \propto \langle \sum_{kbb'} \Xi_{k,k-q}^{bb'} c_{bk}^{\dagger} c_{b'k-q} \rangle \tag{29}$$

Here $\Xi_{k,k-q}^{bb'}$ are matrix elements of the electron−phonon interaction, $c_{bk}^{\dagger}$ and c_{bk} are electron creation and annihilation operators for the state of energy ϵ_{bk}, b is the band index, and k and q are the electron and phonon wave vectors, respectively.

The off-diagonal terms are initially prepared to be nonzero if the duration of the pump pulse is sufficiently shorter than the oscillation period of a phonon mode. Coherent vibrational motion is created in the ground electronic state and is described by a damped oscillator with frequency ω_0, a dephasing time constant $\tau = T_2$, and an initial phase φ.

3.4. Resonant Impulsive Stimulated Raman Excitation vs Displacive Excitation

When the excitation wavelength is resonant with an electronic transition of the system, ISRS excitation (Figure 1, panel (c)) is strongly enhanced. Merlin and co-workers have extended the Raman formalism and successfully explained why the Raman active phonon modes (for example, the E_g mode for Sb) can be coherently excited in addition to the totally symmetric mode (A_{1g}).[31,34] Moreover, they showed that impulsive Raman excitation is applicable to both the transparent (off-resonant) and the opaque (resonant) cases using two separate Raman tensors[34] χ^R and π^R. These tensors are associated with the Raman correction of polarization and the force exerted on the system, respectively. They have the same real component but different imaginary parts. In the off-resonant condition, the real component is responsible for impulsive generation of coherent phonons. In the resonant condition, the imaginary part plays an important role. In contrast to the real component, the imaginary part of π^R is displacive in character because real charge fluctuations associated with photon absorption instantaneously shift the equilibrium position of ions.

The initial phase depends on the detuning of the photon energy with respect to an electronic transition of the system in the impulsive Raman excitation model. By using a time-dependent perturbation method, Chesnoy and Mokhtari[40] showed that the initial phase is determined by

$$\tan \varphi = (\omega - \omega_e) T_e \tag{30}$$

for a molecular system. Here, ω is the optical frequency of the pump pulse, ω_e is the frequency of the electronic transition of the system, and T_e is the electronic dephasing time. When the photon energy is off-resonant, $\varphi = \pi/2$, i.e., an optical pump pulse simply gives an impulsive force to the system, $Q(t) \propto \sin(\omega_0 t) e^{-t/T_2}$. When the photon energy is close to the electronic resonance, a real transition leads to a shift in the equilibrium positions of the ions. Thus, $\varphi \rightarrow 0$, i.e., the ions start to oscillate around this new equilibrium position, $Q(t) \propto \cos(\omega_0 t) e^{-t/T_2}$. The same arguments also hold for adsorbate vibrations and phonons in extended systems.[28,30−32,34] In practice, determining the initial phase of a coherent phonon is sometimes problematic, since the effective start time of the force depends on the carrier dynamics and pump intensity.[41] Moreover, the initial phase depends on the portion of the spectral components of probe pulses to be detected.[42]

When the excitation wavelength is resonant with an electronic transition of the system, the electronic excited state can be populated. As described earlier, coherent oscillations can also be created in the electronic excited state by resonant ISRS (Figure 1, panel (d)), provided that the pulse duration of a pump pulse is substantially shorter than the oscillation period of a vibrational mode in the excited state. In other words, nonzero off-diagonal terms of the density matrix of the electronic excited state are created by the pump pulse field.

The distinction between the evolution of vibrational coherence in the ground and excited states is very clear in the molecular case, since the electronic excitation of a molecule in which electrons are localized in a limited space results in a profound change in the potential energy surface. In contrast, the deformation potentials for ions in solids and on surfaces hardly change upon excitation in the weak excitation limit where the perturbation treatment is valid. Thus, the distinction between the two schemes [panels (c) and (d)] of resonant ISRS may not be practically meaningful in this limit. The distinction would be more clear if the density of excited carriers became so high that the deformation potentials were significantly altered. However, in this strong excitation limit, the perturbation treatment would be no longer valid.

Another mechanism proposed earlier than the resonant ISRS excitation mechanism is displacive excitation of coherent phonons (DECP).[28,30,35] Real populations of elec-

trons in an empty band may change the deformation potential of ions in solids and at surfaces. If a pump pulse produces carriers in an empty band with a sufficiently rapid rising edge that the ions cannot follow the change in the deformation potential and start to oscillate around new equilibrium positions. Note that the oscillator energy is modified through a change in potential energy in the DECP mechanism. In contrast, the kinetic energy is transferred to the oscillator by the real driving force in the case of nonresonant impulsive Raman excitation,[42] as shown in eq 29. The DECP model predicts a cosine-like initial phase of coherent oscillation but only accounts for the generation of totally symmetric phonon modes in the electronic excited state.[28,30]

Since the DECP mechanism is intuitive and simple, this mechanism has been applied to generation of coherent phonons in various semiconductors and semimetals.[35] However, we remark that the electromagnetic field of a pump pulse provides only the energy for electronic excitation from the ground to excited states in the DECP mechanism. This mechanism does not explicitly implement creation of nonzero off-diagonal terms in the density matrix of the system as a source of coherence. In this context, the DECP mechanism is phenomenological. Despite the lack of rigorous treatment for coherence, the DECP mechanism is practical and useful for cases of strong electronic excitation to which the second-order perturbation contributions are no longer applicable.

3.5. Effects of Strong Electronic Excitation

For the strong excitation case, the phenomenological DECP model developed by Zeiger et al.[28] is useful. In this model, only totally symmetric A_1 modes are assumed to be excited coherently. The charge density $n(t)$ in excited bands follows the rate equation

$$\frac{dn}{dt} = \rho I(t) - \beta n(t) \tag{31}$$

where $I(t)$ is the power density of the pump pulse and ρ and β are constants. The first term in eq 31 is the rate of carrier generation in excited bands, and the second term is the rate of electron back transfer to the ground state. The force responsible for the vibration of the A_1 mode is assumed to be proportional to $n(t)$

$$F \propto n(t) \tag{32}$$

By solving the equation of motion, eq 11, with this force, we find that $Q(t) \propto \cos(\omega_0 t)$ for β, $1/T_2 \ll \omega_0$.[28]

This mechanism is analogous to coherent vibrational excitation in excited electronic states of molecules in the gas phase, the evolution of which is monitored by quantum beats in fluorescence decay. In isolated molecules or molecules in a liquid, the ground- and excited-state potential energy surfaces can be clearly distinguished under the Born−Oppenheimer approximation. Quite often the excited-state potential energy surface is displaced from the ground state, and hence an electronic transition in the Franck−Condon fashion creates a nonstationary wave packet on the excited-state potential energy surface.

In bulk solids and at the surface of solids, the two-potential-energy-surface picture cited in the previous paragraph is no longer correct, since electrons form bands of states. As the carrier density increases, the deformation potential of ions is more substantially altered. Thus, the amplitude of a coherent phonon increases with pump power. This is in contrast to the molecular case, in which the amplitude of vibration is determined by the Franck−Condon principle and the number of vibrating molecules increases with the pump power.[28] In addition, if the carrier lifetime is comparable to the dephasing time of coherent phonons, the ions oscillate on the deformation potential wells, which change in time. Therefore, the frequency of coherent phonons may change as they evolve, a process known as "chirping".

A good example of coherent phonons excited by this mechanism is found in the coherent-phonon dynamics of single-crystal Te.[43] The oscillatory frequency of the A_1-mode of Te in time-resolved reflectivity changes decreases linearly with pump power between 3.6 THz (unperturbed phonon frequency) and 3.0 THz. The shifts are interpreted as being due to nonthermal melting of the crystal.

A mechanism similar to DECP called field-screening is frequently quoted in studies of coherent phonons at semiconductor surfaces,[41] which we discuss in Section 6. In the depletion region of semiconductor surfaces, ions oscillate around the equilibrium positions determined by mutual interactions among ions and the electric field associated with the carrier distribution near the surface. When a number of electron−hole pairs are created by absorption of photons, the charge distributions are changed and the injected carriers screen the field. If the carrier injection is fast enough compared with the period of phonon oscillation, ions are displaced with respect to the new equilibrium positions.

4. Real-Time Monitoring Methods

This section describes the monitoring of coherent vibrations and phonons at surfaces. Once coherent oscillations are generated by the mechanisms described in the previous section, oscillating macroscopic polarizations are created. Thus, the dynamics of coherent vibrations can be probed by monitoring the time-evolution of the macroscopic polarization. The time-domain spectroscopy methods described here are based on second-order nonlinear optical processes, including time-resolved sum frequency generation (TRSFG) and time-resolved second harmonic generation (TRSHG). We first summarize the basics of nonlinear optical response in Section 4.1 and then describe each spectroscopy method in the following Sections 4.2 and 4.3.

4.1. Basics of Nonlinear Spectroscopy

This section covers only the basics of nonlinear spectroscopy helpful in understanding the time-domain measurements described in this review. For a deeper understanding, refer to the many excellent books on nonlinear spectroscopy.[19,37,38]

When an optical field $E(t)$ is applied to a material, macroscopic polarization $P(t)$ is generated. When the electric field strength is substantially large, $P(t)$ shows nonlinear dependence on $E(t)$. Corresponding to the perturbation approach in eq 17, the time-dependent polarization $P(t)$ can also be expanded as

$$P(t) = P^{(1)}(t) + P^{(2)}(t) + P^{(3)}(t) + \cdots \tag{33}$$

with

$$P^{(n)}(t) = \mathrm{Tr}\{V\rho^{(n)}(t)\} \tag{34}$$

where V is the dipole operator and $P^{(n)}$ is the nth order

polarization. Here we assume no permanent polarization in the media, i.e., $P^{(0)} = 0$.

These terms can also be written using the linear $\chi^{(1)}$ and nth order nonlinear susceptibilities $\chi^{(n)}$ ($n \geq 2$), such as

$$P^{(i)} = \chi^{(i)}E^{i}(t) \tag{35}$$

Time-varying polarization can act as a source of radiation. The radiation propagates in media with refractive index n following the Maxwell wave equation

$$\nabla^2 E - \frac{n^2}{c^2}\frac{\partial^2 E}{\partial t^2} = \frac{4\pi}{c^2}\frac{\partial^2 P^{(i)}}{\partial t^2} \tag{36}$$

where c is the speed of light in a vacuum.

Here we represent the optical field with frequency ω_k as

$$E_k(t) = E_k e^{-i\omega_k t} + \text{c.c.} \tag{37}$$

The second-order nonlinear polarization created by two kinds of optical fields $E_1(t)$ and $E_2(t)$ is given according to eq 34 as

$$P^{(2)} = \frac{1}{2}\sum_n P(\omega_n)e^{-i\omega_n t} \tag{38}$$

where the summation extends over positive and negative frequencies ω_n. The polarization terms include various frequency components, including the second harmonic $2\omega_i$ ($i = 1, 2$) and sum frequency $\omega_1 + \omega_2$,

$$P(2\omega_i) = \chi^{(2)}E_i^{\,2} \tag{39}$$

$$P(\omega_1 + \omega_2) = 2\chi^{(2)}E_1E_2 \tag{40}$$

Note that the second-order susceptibility vanishes when the system possesses inversion symmetry. Since $\chi^{(2)}$ is inherently nonzero at surfaces and interfaces where inversion symmetry is broken, second-order nonlinear spectroscopy is sensitive to surfaces and interfaces.

When the system has a restoring force given by

$$F_r = -m'\omega_0^{\,2} - m'aQ \tag{41}$$

the equation of motion in the model based on classical forced oscillators, given by eq 11, is modified as

$$\frac{d^2}{dt^2}Q + \frac{2}{T_2}\frac{d}{dt}Q + \omega_0^{\,2}Q + aQ^2 = \frac{F(t)}{m'} \tag{42}$$

Here the parameter a represents anharmonicity. Under the force $F(t)$ exerted on the system by the interaction with the radiation field,

$$F(t) = -e^*E(t) \tag{43}$$

the second-order susceptibility can be expressed as

$$\chi^{(2)}(2\omega_2) = \frac{-a(e^*/m')^2E_2^{\,2}}{D(2\omega_2)D^2(\omega_2)} \tag{44}$$

$$\chi^{(2)}(\omega_1 + \omega_2) = \frac{-2a(e^*/m')^2E_1E_2}{D(\omega_1 + \omega_2)D(\omega_1)D(\omega_2)} \tag{45}$$

where we have introduced the complex denominator function

$$D(\omega_j) = \omega_0^{\,2} - \omega_j^{\,2} - 2i\omega_j/T_2 \tag{46}$$

These second-order processes play a central role in the detection of coherent vibrational motions at surfaces and interfaces; we describe sum frequency generation in Section 4.2 and SHG in Section 4.3 in more detail.

4.2. Time-Resolved Sum Frequency Generation

By using an IR pulse for one of the impinging lasers in sum frequency generation (SFG) measurements, SFG becomes a very powerful tool for monitoring the vibration of adsorbates on surfaces. As shown in eqs 45 and 46, if the IR frequency ω_{IR} is in resonance with a vibrational mode, i.e., $\omega_{IR} = \omega_0$, the SFG amplitude is resonantly enhanced.

SFG has been demonstrated to be a very powerful vibrational spectroscopic tool for molecules on surfaces.[44−47] This technique has been applied to well-defined single-crystal surfaces as well as liquid−metal interfaces in electrochemical systems.[48] Because SFG is based on second-order nonlinear processes, it is also surface sensitive, as in the case of SHG. Furthermore, in combination with an ultrafast pump laser, SFG provides an excellent opportunity for time-resolved vibrational spectroscopy.

In contrast to linear spectroscopy methods, such as infrared reflection absorption spectroscopy (IRAS), the analysis of SFG spectral lines is rather complicated. When IR radiation with a frequency of ω_1 and visible light with a frequency of ω_2 are mixed at a sample surface, macroscopic polarization with frequency $\omega = \omega_1 + \omega_2$ is generated

$$P^{(2)}(\omega) = \chi^{(2)}(\omega = \omega_1 + \omega_2)E_{\text{IR}}(\omega_1)E_{\text{VIS}}(\omega_2) \tag{47}$$

As shown in eqs 45 and 46, $\chi^{(2)}$ has a resonant term $\chi_R^{(2)}$ with respect to a vibrational transition at ω_0,

$$\chi_{\text{R}}^{(2)} = \frac{B}{(\omega_1 - \omega_0) - i\gamma} \tag{48}$$

where γ is the inverse of the total dephasing time T_2 of the vibrational mode, and B is a constant. In addition to the resonant term, $\chi^{(2)}$ includes a nonresonant term $\chi_{\text{NR}}^{(2)}$; thus

$$\chi^{(2)} = \chi_{\text{NR}}^{(2)}e^{i\phi} + \chi_{\text{R}}^{(2)} \tag{49}$$

Here ϕ is the relative phase between the resonant and nonresonant terms. Thus, SFG spectra can be written as

$$I(\omega) \propto |\chi_{\text{NR}}^{(2)}e^{i\phi} + \chi_{\text{R}}^{(2)}|^2 \tag{50}$$

If χ_{NR} is not negligible, the SFG spectral lines are not necessarily symmetric but can be asymmetric due to the interference between the two terms.

In early SFG studies, measurements were made with a combination of ps-IR and visible pulses. In this mode, SFG spectra are obtained by monitoring the SFG signals, while the frequency of the IR pulse is scanned in the range of interest. The energy resolution is mainly determined by the frequency width of the IR laser pulses.

More recently, it has become more common to use an intense broad band femtosecond-IR laser source.[49] Richter and co-workers[50] demonstrated that SFG spectra can be obtained over a 400-cm^{-1} spectral region without scanning

the IR frequency. In this mode, SFG signals are generated by mixing the broad band femtosecond-IR pulse with a narrow band visible laser pulse at the sample surface. The SFG signals are dispersed with a spectrograph and detected simultaneously by a sensitive CCD detector. Broad band tunable IR pulses are generated by difference frequency mixing of the signal and the idler of an optical parametric amplifier in an appropriate crystal such as $AgGaS_2$. The spectral resolution of this method is determined by the spectrograph and the bandwidth of the visible pulse. In combination with the parallel CCD detection, the entire SFG spectrum can be recorded and averaged. This approach is more efficient than the scanning mode for recovering SFG spectra, because the data acquisition rates are substantially enhanced and the time resolution is better. More importantly, since the entire spectral region is recovered simultaneously, this method does not show contamination or degradation during scanning often seen in the earlier SFG spectroscopy method.

However, caution is required in analyzing the line shapes of SFG spectra taken with broad band IR and narrow band visible laser pulses.[51−54] In this case, frequency-domain analysis based on the line shape given by eq 50 is not suitable. Rather, it is more appropriate to analyze the spectra by the Fourier transform of the time-dependent polarization:

$$I_{\mathrm{SFG}}(\omega, t_{\mathrm{d}}) \propto \left|\int \mathrm{d}t e^{i\omega t} P_{\mathrm{IR}}(t, t_{\mathrm{d}}) E_{\mathrm{VIS}}(t)\right|^2 \qquad (51)$$

Here $P_{\mathrm{IR}}(t, t_{\mathrm{d}})$ is the time-dependent polarization at a delay time between IR and visible pulses of t_{d},

$$P_{\mathrm{IR}}(t, t_{\mathrm{d}}) = \chi(t; t_{\mathrm{d}}) E_{\mathrm{IR}}(t) \qquad (52)$$

If the time duration of the visible pulse is substantially longer than the dephasing time, this treatment gives the same expression in the frequency domain. However, if the duration of the visible pulse is shorter than the dephasing time, the duration determines the window for observing the time-dependent polarization $P_{\mathrm{IR}}(t, t_{\mathrm{d}})$. Thus, the SFG spectral line shapes measured by this method depend in principle on the time delay between the IR and visible pulses and the duration of the visible pulse. Figure 2 shows the SFG spectral lines of the stretching mode of CO on Pt(111) simulated by these parameters. As shown in Figure 2b, the spectral line narrows as the duration of the visible pulse increases. When the duration of the visible pulse is fixed (Figure 2c), the spectral width narrows with increase of the delay because the overlap between $P_{\mathrm{IR}}(t, t_{\mathrm{d}})$ and the visible pulse increases as the visible pulse is delayed from the IR pulse.

In the case of IR-pump and SFG-probe measurements, the pump pulse induces a time-dependent polarization $P_{\mathrm{IR}}(t)$, which is further modulated by the IR-probe pulse. Thus, the effects of the pump and probe IR pulses have to be taken into account explicitly in the time domain.[53]

4.3. Time-Resolved Second Harmonic Generation

When a coherent oscillation is created at a surface by a pump pulse via one of the excitation mechanisms described in Section 3, the second-order optical susceptibility $\chi^{(2)}(2\omega_i)$ and hence the polarization $P(2\omega_i)$ are modulated by the coherent oscillation. Thus, the time-evolution of the coherent oscillation can be detected by measuring the second harmonic intensity converted from the probe pulse as a function of pump−probe delay. This detection method can be described

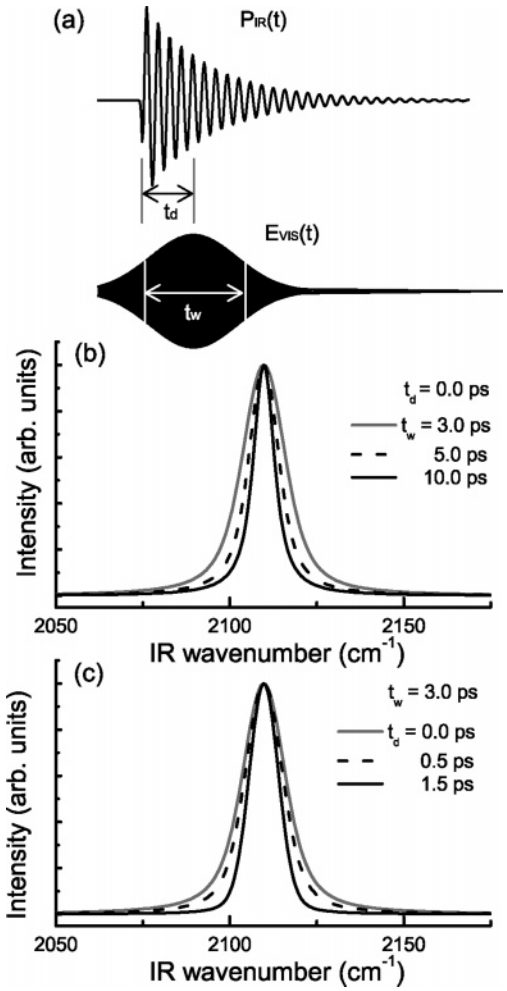

Figure 2. Simulations of the SFG spectral line shape of the stretching mode of CO on Pt(111): (a) time-dependent polarization induced by a broad band IR pulse $P_{\mathrm{IR}}(t)$, depicted in upper trace, and electric field of the visible pulse $E_{\mathrm{VIS}}(t)$ with duration t_{w}, in lower trace. The latter pulse is delayed by t_{d} from the IR pulse. Simulated line shapes are shown in (b) as a function of t_{w} at a fixed $t_{\mathrm{d}} = 0$ ps and (c) as a function of t_{d} at a fixed $t_{\mathrm{w}} = 3$ ps.

as the coherent time-domain analogue of stimulated hyper-Raman spectroscopy. It was first applied to the study of coherent phonons at semiconductor surfaces by Tom and co-workers,[55] as described in more detail in Section 6. If surface coherent phonons are created by the ISRS excitation (Section 3.3), it is more rigorous to describe the whole process including excitation and detection as stimulated hyper-Raman scattering ($\chi^{(4)}$ process).[56] Since creation of coherent phonons can be modeled by various mechanisms other than ISRS, as described in Section 3, we describe detection by the $\chi^{(2)}$ process in this review.

We expand $\chi^{(2)}$ in terms of the vibration (or phonon) coordinate of interest Q_j,

$$\chi^{(2)} = \chi_0^{(2)} + \frac{\partial \chi^{(2)}}{\partial Q_j} \cdot \delta Q_j + \cdots \qquad (53)$$

Since the intensity of second harmonic radiation $I_{\mathrm{SHG}}(2\omega)$ is proportional to $|\chi^{(2)}(2\omega)|^2$, $I_{\mathrm{SHG}}(2\omega)$ can be expressed in terms of $\chi_0^{(2)}$, independent of Q_j, and $\chi_Q^{(2)}$, dependent on Q_j, as

$$I_{\mathrm{SHG}}(2\omega) \propto |\chi_0^{(2)}|^2 + |\chi_Q^{(2)}|^2 + 2\mathrm{Re}[\chi_Q^{(2)} \cdot \chi_0^{(2)}] \qquad (54)$$

Here, the first term is a constant contribution to the second harmonic intensity, while the second and third terms represent signals modulated by the coherent oscillation. Usually the modulation amplitude due to $|\chi_Q^{(2)}|$ is small, and thus the contribution from the second term is negligible. In contrast, the third cross term can be large enough to be detected if $\chi_0^{(2)}$ is substantially large. Therefore, the detection of modulated signals as a function of pump−probe delay in TRSHG relies on a heterodyne detection method. This condition is satisfied for the measurement of coherent surface phonons on GaAs surfaces (Section 6.1) and alkali-atom covered metal surfaces (Section 7.3). In the former case, because GaAs crystals do not possess inversion symmetry, second harmonic radiation is generated even from the bulk crystals, and the conversion to the second harmonic is very large. In the latter case, the intensity of second harmonic radiation is dramatically increased by the enhancement of the local field created by alkali-atom adsorption and/or electronic resonant transitions in the metallic quantum well. See later sections for more details.

The experimental setup of TRSHG is relatively simpler than that of TRSFG. Either the oscillator or regenerative amplifier of a Ti:sapphire laser is usually used for the light source. The output beam of the laser is split into two for the pump and probe pulses. The two pulses are overlapped spatially at the sample surface. The second harmonic intensity of the probe pulse is measured as a function of pump−probe time delay. An optical chopper is inserted in the optical path of the pump beam and the modulations in the second harmonic intensity of the probe beam $\Delta I_{SHG}(t)$ are recovered by lock-in detection or by directly subtracting the second harmonic intensity without a pump pulse from that with a pump pulse.

TRSHG traces showing modulation signals due to coherent oscillations created by pump pulses can be analyzed by fitting the oscillatory part to multiple underdamped oscillating functions:

$$\Delta I_{SHG}(t) = \sum_i A_i \cos(\omega_i t + \varphi_i) e^{-\gamma_i t} \qquad (55)$$

Another fitting method for TRSHG traces is linear prediction singular value decomposition (LPSVD).[57,58] In this method, each data point is assumed to be a linear combination of a finite number of previous data points. This assumption is satisfied if the transient signals are a linear combination of exponentially damped sinusoids. Under this assumption, the resulting set of equations for each data point is represented by a matrix that can be solved by a linear least-squares fitting procedure. This technique is powerful and avoids the inherent difficulties associated with nonlinear least-squares fitting by recasting the problem as sequential linear least-squares fits.

5. Coherent Vibration and Dephasing of CO on Metal Surfaces

Carbon monoxide is the cornerstone adsorbate for studies on adsorbate−substrate interactions on metal surfaces. CO also plays an important role in studies on vibrational relaxation on metal surfaces. The strong oscillator strength of the CO internal stretching mode (ν_1) on metals allows the line shape and temporal response to be studied for wide ranges of coverage and temperature. Many studies have been conducted by frequency- and time-domain spectroscopy on the vibrational relaxation of the ν_1 mode on various metal surfaces. We first describe the electronic structure of CO on metal surfaces in Section 5.1, then in Section 5.2 we summarize briefly the important findings on the vibrational relaxation of the ν_1 mode of CO on metal surfaces from studies conducted by the mid 90's. The works cited in Section 5.2 are not exhaustive, and readers should refer to the several excellent reviews on the analysis of line profiles obtained by IRAS[3,59] and the pump−probe approaches using resonant picosecond infrared pulses for excitation of the CO ν_1 mode performed in the mid 90's.[5,6] More recent progress in time-domain spectroscopy on this subject has been reviewed by Ueba.[7] Having reviewed the electronic structure and vibrational relaxation of CO on metal surfaces, we focus on the most recent progress made on this subject in studies with femtosecond pulsed lasers in Sections 5.3 and 5.4.

5.1. Electronic Structure of CO on Metal Surfaces

The adsorption of CO on metal surfaces can be qualitatively understood by the Blyholder model,[60] i.e., σ-electron donation from CO to the vacant conduction band of the metal and π-electron back-donation from the metal bands to the vacant $2\pi^*$ orbital of CO. The redshift of the CO stretching frequency from 2170 cm^{-1} for free CO is attributed to the electron back-donation to the $2\pi^*$ antibonding state of CO. The CO stretching frequency is very sensitive to the adsorption site, such as atop, bridge, and 3-fold hollow sites, which is a good indicator of the electronic and structural properties at the local site where CO is adsorbed.

On the basis of X-ray emission spectroscopy measurements in combination with density functional theory calculations, Nilsson and co-workers[61,62] suggested that the CO orbitals and the metal bands are significantly hybridized. Orbital mixing among the CO 1π and $2\pi^*$ bands and the metal d_π-band is responsible for the weakening of the internal CO bond and contributes to the attractive interaction with the metal surface. Orbital mixing between the internal CO σ-band and the metal d_σ-band strengthens the internal CO bond and contributes to the repulsive interaction with the surface. Thus, they concluded that the balance between the π and σ interactions determines the vibrational frequency and the adsorption energy of CO.

The unoccupied state of atop CO band on Pt(111) has been identified at 4.3 eV above the Fermi level E_F by inverse photoemission[63] and two-photon photoemission.[64] It has been assigned to the $2\pi_a^*$ state. However, the lowest unoccupied electronic state caused by the hybridization between the 5σ-band and the metal bands has not been detected by those methods. Chou et al.[65] have recently identified this unoccupied state of CO on Pt(111) by using SFG spectroscopy with a tunable visible laser. CO is adsorbed at both atop and bridge sites of Pt(111) or Pt(110). The absorption bands of the ν_1 modes of CO at both sites can be clearly observed by IRAS. In SFG spectra, in contrast, although the intensity of the stretching band of CO at the atop site of Pt(111) is prominent, that of CO at the bridge site is either very weak or almost missing on Pt(110).[66] Chou et al. have shown that the SFG intensity of the stretching mode of atop CO is enhanced in the visible photon energy range between 2.2 and 2.6 eV. Note that $\chi^{(2)}$ responsible for SFG is also resonantly enhanced if the visible photon energy is tuned to an electronic transition as shown in eqs 45 and 46. Thus, the observed resonance feature in the SFG intensity associated with the ν_1 mode, peaking at 2.51 eV with a bandwidth of 0.83 eV, can be attributed to the transition from the

occupied $2\pi^*_b$ state at 0.3 eV below E_F to the unoccupied state at 2.2 eV above E_F. The unoccupied state has been assigned to the $5\sigma_a$ state, derived from the hybridization of Pt 6*sp* and CO 5σ. In contrast to CO on the atop site, since CO at the bridge site is more strongly bound to the surface, the amount of redshift of the ν_1 mode is larger. Because of the stronger interactions with the substrate, the $5\sigma_a$ state of bridge CO is expected to be located at a higher energy than that of atop CO. Therefore, a UV input is required to enhance the SFG intensity of the ν_1 band of bridge CO. Usually SFG experiments are performed with a visible input with a fixed energy. Thus, the SFG detection of the ν_1 mode of bridge CO is electronically off-resonant and less sensitive than that of atop CO.

5.2. Vibrational Relaxation Mechanisms

5.2.1. Electron-Hole Pair Excitation

As described in Section 2, vibrational relaxation includes contributions from population decay (T_1 process) and pure phase relaxation (T_2* process). We focus first on population decay. There are two major population decay channels for a vibrationally excited molecule at a surface: emission of phonons and electron−hole excitation. In contrast to adsorbates on insulators and semiconductors with a wide band gap, where population decay by multi-phonon generation is the major decaying path, electron−hole pair excitation plays an important role in population decay on metal surfaces.

The important role of electron−hole pair excitation was suggested by Persson and Persson[67] based on their theoretical treatment. Their theory assumes that the CO stretching motion couples with the charge oscillation between the metal and CO $2\pi^*$ orbitals. The estimated lifetime of the CO stretching vibrational mode for CO on a Cu(100) surface is in reasonable agreement with that obtained from the line width of the IR absorption band. The effects of electron−hole pair excitation on the line shape have been investigated further in theoretical studies.[21,68] On the other hand, the population decay lifetime has been estimated more precisely by experiment. Ryberg has measured the line shape of the infrared absorption band of the CO stretching mode in the $c(2 \times 2)$ configuration on Cu(100) and showed that the intrinsic line width is 4.6 cm^{-1} full width at half-maximum (fwhm).[69] This sets the lower limit of T_1 to be 1.2 ps. In contrast, a longer lifetime was estimated by Harris and coworkers with ps-IR pump and SFG-probe spectroscopy.[70] By measuring the normalized transient response of SFG signals of the ν_1 mode after excitation by an intense IR resonance pulse, they determined the lifetime to be 2.0 ps, longer than that estimated from the line width measurements. The discrepancy has been attributed to inhomogeneous spectral broadening or insufficient resolution in the frequency-domain measurements. The measured lifetimes agree reasonably well with the theoretical predictions where the nonadiabatic energy transfer lifetime to electron−hole pair excitation was calculated to be in the range of 1−3 ps.[71,72]

5.2.2. Dephasing

While electron−hole pair excitation is an important pathway for population decay on metal surfaces, pure dephasing also contributes significantly to the vibrational dephasing of CO on metal surfaces. Strong temperature dependence of the line shape of the ν_1 band has been found for CO on Ni(111),[73,74] Ru(001),[22] and Pt(111).[75] Since decay via electron−hole pair excitation is practically temperature independent,[76,77] the strong temperature dependence was attributed to pure dephasing. Persson and Ryberg[74] developed a theory incorporating pure dephasing due to anharmonic coupling between the ν_1 mode and low-frequency modes such as frustrated translation (ν_4) and rotation (ν_3).

Although it has been reported that the line width is independent of temperature on Cu(100) in an early study,[69] Germer et al. performed careful line shape measurements by IRAS and clearly showed that the ν_1 band shifts to lower frequency and broadens as the temperature is raised from 90 to 160 K.[78] This was interpreted as being evidence of exchange dephasing[22,79,80] by the frustrated translation mode ν_4. Namely, anharmonic coupling of ν_1 with ν_4 populates the frustrated translation mode whose population fluctuates due to the exchange of energy with the substrate. In this model, the frequency ν_1 and width $\delta\nu_1$ of the ν_1 band are given by[22,80]

$$\nu_1 = \nu_1^{\,0} - \Gamma_{14}\langle n_4(T)\rangle \tag{56}$$

$$\delta\nu_1 = \delta\nu_1^{\,0} + \frac{2(\Gamma_{14})^2}{W}\langle n_4(T)\rangle\langle n_4(T)+1\rangle \tag{57}$$

Here, $\nu_1^{\,0}$ and $\delta\nu_1^{\,0}$ are the frequency and the line width at $T = 0$ K, respectively, Γ_{14} is the anharmonic coupling between the ν_1 and ν_4 modes, $\langle n_4(T)\rangle$ is the average occupation in ν_4, and W is the frequency width parameter. The simultaneous fitting of the frequency and line width data for $\nu_4^{\,0} = 32$ cm^{-1} provides $\Gamma_{14} = 1.4$ cm^{-1} and $W = 87$ cm^{-1}. This exchange model has also been successfully applied to the temperature dependence on other surfaces including Pt(111),[80,81] Ru(001),[22] and Ni(111).[22,74]

In the works cited so far, the coupling between ν_1 and lateral vibrational modes (ν_3 and ν_4) were extracted from the temperature dependence of the line shape of the ν_1 band. In addition, the frustrated translation mode ν_4 of CO on Cu(100) was directly observed by high-resolution helium atom scattering.[82] Graham et al. observed systematic frequency shifts and line broadenings of this mode as a function of temperature. These results were attributed to the growing hot bands of the translational modes whose frequencies are redshifted by the anharmonicity of the lateral CO−Cu potential curve. Alternatively, anharmonic coupling between the nearly 2-fold degenerate translational modes can cause the line shape variations observed. The line width extrapolated to $T = 0$ corresponds to a lifetime of 8 ps, which is a factor of 2 longer than the lower limit of T_1 deduced from the temperature dependence of the line width of the ν_1 absorption band. Since the measurements were performed with very small coverage $\theta \leq 6\%$ of $c(2 \times 2)$, this discrepancy was attributed to lateral adsorbate−adsorbate interactions that reduce the lifetime significantly at high coverage.

5.3. Localization vs Delocalization

When adsorbates are isolated from each other, the vibrational modes of an adsorbate are well localized in the adsorbate and vibrationally excited states of the adsorbate relax by interactions with the substrate. As interactions between adsorbates increase, the vibrational modes of adsorbates couple with each other and form bands, i.e, the vibrational modes are delocalized. An adsorbate undergoes a reaction once the intra-adsorbate, adsorbate−adsorbate,

and/or adsorbate−substrate vibrational modes relevant to the reaction are excited to overcome the activation barrier. Thus, a vibrational mode relevant to the reaction has to be excited sufficiently for the reaction to occur. In this context, it is important to know how a localized adsorbate vibration becomes delocalized for an understanding of vibrational energy migration and chemical reactions on surfaces.

Note that a similar problem exists even for isolated molecules in the gas phase. From the viewpoint of reaction control via selective vibrational excitation,[83−85] it is vital to know how to excite a specific bond (or local mode) of a molecule sufficiently and how fast the energy in the bond is delocalized in the molecule. Anharmonic couplings between normal modes are much better characterized for isolated molecules,[86] and the dynamics of "delocalization" due to anharmonic couplings have been extensively studied and are known as the issue of intramolecular vibrational redistribution.[87,88]

The transition between localization and delocalization of a vibrational mode can be understood qualitatively by comparing the vibrational anharmonicity Γ with the phonon bandwidth W.[89] If $W < \Gamma$, the vibration mode will be well localized in the adsorbate, whereas if $W > \Gamma$, the vibration mode of the adsorbate will be delocalized.

A critical test for localization vs delocalization of adsorbate vibrations is to observe the higher vibrationally excited states ($\upsilon \geq 2$). If the vibration is well localized, it is in principle possible to observe overtone and/or hot bands of the mode of interest. The observation of these bands provides the anharmonicity of a potential curve with respect to the vibrational coordinate.

In contrast to the great amount of information on vibrational relaxation of the first vibrationally excited state of the CO ν_1 mode on metals described earlier, very little is currently known on higher vibrationally excited states. This is due to serious sensitivity problems of vibrational spectroscopy for adsorbates.[90−93] The intensities of overtone bands are typically 2 or 3 orders of magnitude weaker than those of fundamental bands. Overtone spectroscopy is made very difficult by the inherently small transition probabilities in addition to severe limitations on the detection sensitivities of conventional vibrational spectroscopy methods, such as high-resolution electron energy loss spectroscopy (HREELS) and IRAS.

Despite the difficulties, Jakob has successfully observed the overtone of the ν_1 band of CO[94] and the combination band of ν_1 and the Ru−CO stretching mode[95] of $(\sqrt{3} \times \sqrt{3})$CO on Ru(001) by IRAS. The anharmonicity of the ν_1 mode was found to be about 40% larger than that for gas-phase CO, which makes it possible to form a well-defined two-phonon bound state outside the continuum of delocalized states.

The line width of the overtone of ν_1 increases rapidly with increasing surface temperature, compared with that of the fundamental band. This is attributed to the decay of the localized two-phonon bound state into single phonon states.[94] Jakob and Persson[95] performed a detailed analysis of the vibrational line shape of the combination and overtone bands. They found that dynamic lateral interactions cause severe line shifts of the overtone bands. The anharmonicity of the ν_1 mode was revised to be 27 cm^{-1} when the lateral interactions were taken into account. Furthermore, they showed that the energy relaxation rate for the overtone is twice as large as for the fundamental band, while the pure dephasing rate is approximately four times larger than that of the fundamental excitation, provided that the population and pure dephasing of the overtone are dominated by the same adsorbate−substrate coupling terms as for the fundamental mode. In addition to CO/Ru(001), the overtones of the internal stretching mode of NO on Ru(001) and oxygen-covered Ru(001) were observed.[96] The overtone bands also show broadening, about four times faster than the fundamental band as the surface temperature increases. This temperature dependence was also well accounted for by the model applied to CO/Ru(001).

Another way to access two-phonon bound states is sequential pumping of vibrational states of adsorbates by intense IR pulses: $\upsilon = 0 \rightarrow 1$ and $\upsilon = 1 \rightarrow 2$. This scheme can be naturally adapted by time-domain measurements with a combination of intense IR pump and SFG probe pulses. In particular, as described in subsection 4.2, second generation SFG spectroscopy[50] with broad band IR and narrow band visible pulses provides higher sensitivity than conventional SFG measurements with ps-IR and visible laser pulses, which makes it possible to observe the two-phonon bound state of CO on Ru(001).[53]

Time-resolved measurements of free induction decay of IR-polarization for 0.33 ML CO on Ru(001) have been performed.[53] The TRSFG signals show a single-exponential decay over three decades with a dephasing time of $T_2 = 1.94$ ps at 95 K and $T_2 = 1.16$ ps at 340 K. The dephasing times are consistent with pure homogeneous broadening due to anharmonic couplings with thermally activated low-frequency lateral modes together with a contribution from saturation of the IR transition.

Hess et al.[97] also observed the hot-band transition of $\upsilon = 1 \rightarrow 2$ of CO on Ru(001) by intense broad band-IR pump and SFG probe measurements and determined the anharmonicity constant from the frequencies of both the fundamental and the hot-band transitions. Note that the high sensitivity of this method allows detection as low as 0.001 ML of CO. The fwhm of the fundamental transition is 8.4 cm^{-1}, while that of the hot band is 14.5 cm^{-1} at a coverage of 0.04 ML. Although saturation due to intense IR excitation pulses affects the line shape of the SFG spectra, the large line width of the hot band implies that the $\upsilon = 2$ vibrational state relaxes much faster than the lowest excited state. The temperature dependence of the dephasing of the $\upsilon = 1 \rightarrow 2$ transition was further investigated to extract pure dephasing contributions.[98] As a result, despite the marked difference in the line width, the contribution to the line width from anharmonic coupling to the low-frequency frustrated translational mode is identical for both $\upsilon = 0 \rightarrow 1$ and $\upsilon = 1 \rightarrow 2$. Since anharmonic coupling is expected to be larger for higher vibrationally excited states, it is rather surprising that the anharmonic coupling between the internal CO stretching mode and the low-frequency modes is independent of the degree of vibrational excitation in ν_1. Information on anharmonic coupling of highly excited vibrational states of adsorbates is still very rare. Thus, we need to await more works to answer the questions including how anharmonic coupling depends on vibrational quanta and modes.

Hess et al.[99] demonstrated delocalization of the localized CO-stretching vibration on Ru(001) by measuring SFG spectra as a function of CO coverage. As shown in Figure 3, both the fundamental and the hot bands are discernible at 0.006 ML, but the hot band decreases with increased coverage and the two bands merge into a broad single peak,

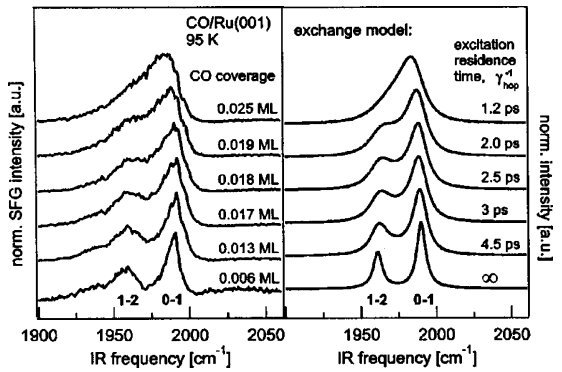

Figure 3. SFG spectra of the ν_1 mode of CO on Ru(001) as a function of coverage at 95 K. The left panel depicts the observed spectra, showing that the $n = 1 \rightarrow 2$ hot band decreases and disappears at a coverage of 0.025 ML. The right panel depicts the spectra simulated by the exchange model for varying excitation residence times. Reprinted with permission from ref 101. Copyright 2001 American Institute of Physics.

indicating that a transition from the discrete vibrational energy structure to a continuum of states takes place at a coverage of CO as low as 0.025 ML. The spectra were well fitted by the spectral line shape function of the exchange model[79,100] and the hopping rate of the vibrational excitation was estimated to be less than 2.5 ps^{-1}, later revised[101] to 1.2 ps^{-1}. This indicates that vibrational energy transfer among adsorbates is as effective as energy decay into the substrate.

Vibrational energy transfer within adsorbates owing to dipole−dipole interactions on Ru(001)[101] was further modeled by a Förster-type energy transfer mechanism.[102] The rate of energy transfer $k_{d\rightarrow a}$ from an excited donor dipole to an unexcited acceptor dipole can be written as

$$k_{d\rightarrow a} = \frac{\kappa^2 \mu_d^2 \mu_a^2}{4n^4 \epsilon_0^2 h^2 c r^6} \int_0^\infty g_d(\nu) g_a(\nu) d\nu \qquad (58)$$

where ϵ_0, h, and c are the vacuum permittivity, Planck's constant, and the velocity of light, respectively, μ_d and μ_a are the absolute values of the transition dipole moments of the donor and acceptor, r is the distance between the dipoles, n is the refractive index of the medium, $g_d(\nu)$ and $g_a(\nu)$ are the normalized homogeneous line shapes of the donor and acceptor vibrations, respectively, and κ is a geometric factor. As cited earlier, since the absorption line of the ν_1 mode of CO on Ru(001) can be represented by a Lorentzian profile with a homogeneous width of $\delta\nu_{hom}$, the spectral overlap integral can be replaced by $1/\pi\delta\nu_{hom}$. This leads to

$$k_{d\rightarrow a} = \frac{3.01 \times 10^{17}}{r^6} \qquad (59)$$

with r in Å. For $\theta = 0.025$ ML, where the transition from localized vibration to delocalized phonons is completed, the rate of energy transfer is estimated to be $(80\ ps)^{-1}$ with an average distance $\langle r \rangle = 17$ Å. This is much slower than the value of $(1.2\ ps)^{-1}$ obtained from fitting with the exchange model. However, there will be a statistical distribution of the intermolecular distances. Thus, molecules close to each other contribute largely to energy transfer owing to the r^{-6} dependence. Considering the statistical distribution of intermolecular distances on the surface, the average rate $\langle k_{d\rightarrow a} \rangle$ was estimated to be $(0.3\ ps)^{-1}$. This value is in reasonable agreement with that obtained from fitting with the exchange model. Thus, it was concluded that the vibrational energy transfer among CO on Ru(001) is well explained by the Förster model.

Similar measurements were performed for CO adsorbed on Ir(111) by King and co-workers.[103] A striking difference to CO on Ru(001) is the coverage at which the hot band transition is no longer discernible, i.e., 0.11 ML on Ir(111) in comparison with 0.025 ML on Ru(001). The Förster model predicts the rate of energy transfer to be $(8.9\ ps)^{-1}$ at 0.24 ML. Although the lifetime for CO on Ir(111) is not known, if it is assumed that vibrationally excited CO on Ir(111) decays with a similar rate as 0.3 ML CO on Pt(111),[104] i.e., $(2\ ps)^{-1}$, this transfer rate seems much slower than the energy decay to the substrate. Since merging of the fundamental and hot bands occurs on the surface at much higher coverage, this calculated slow exchange rate appears reasonable for this system. The frequencies of both fundamental and hot bands show significant blue shifts at 0.08 ML, indicating that dipole−dipole coupling occurs at this coverage. This coverage is well below that at which the two transitions merge. In contrast, blue shift occurs on Ru(001) at approximately 0.05 ML,[101] which is larger than the coverage of 0.025 ML at which merging of the hot band with the fundamental band is completed. Thus, King and co-workers raised the question as to why the two bands merge before dipole−dipole coupling occurs for CO/Ru(001). Currently, it is not clear why CO behaves differently on these surfaces.

5.4. Inter-Adsorbate Interactions

As discussed in the previous subsection, inter-adsorbate interactions become effective as the adsorbate coverage increases. The interactions manifest as changes in the shape of vibrational spectral lines and the relaxation rates. However, it is difficult to disentangle the contributions to the inter-adsorbate interactions from these changes. Two-dimensional (2-D) vibrational spectroscopy using a $\chi^{(3)}$ nonlinear optical process has been investigated theoretically[105,106] for extracting information on the intra- and inter-adsorbate vibrational mode couplings. 2-D vibrational spectroscopy has previously been applied to probe coupling of vibrational modes in liquids[107] and protein.[108]

Bonn and co-workers demonstrated IR−IR−visible SFG spectroscopy applied to CO on Ru(001).[109] The upper panel of Figure 4 shows conventional IR−visible SFG spectra. The spectral line of the CO stretching vibration is strongly enhanced compared with the nonresonant background. An extra peak appearing at around 4040 cm^{-1} can be seen in the lower panel. This sharp peak cannot be due to the overtone of the ν_1 mode, since the overtone should appear at 3940 cm^{-1} because of its anharmonicity. The frequency of 4040 cm^{-1} is twice the frequency of the fundamental transition at 2020 cm^{-1}. Furthermore, the temperature dependence of the frequency ω and the width $\delta\omega$ of the line can be described quite well with $\omega = 2 \times \omega_{01}$ and $\delta\omega = 2 \times \delta\omega_{01}$, where ω_{01} and $\delta\omega_{01}$ are the frequency and width of the fundamental transition, respectively. The peak at 4040 cm^{-1} could be due to two cascaded $\chi^{(2)}$ processes. However, this is unlikely, because the radiated IR−visible SFG field is too weak to be able to create a cascaded IR−IR−visible signal. Furthermore, the cascaded processes cannot explain the observed coverage dependence. Thus, this peak is interpreted in terms of two $v = 0 \rightarrow 1$ transitions due to a direct $\chi^{(3)}$ process as follows.

Theoretically this process is described as a four-wave mixing process with the third-order nonlinear susceptibility

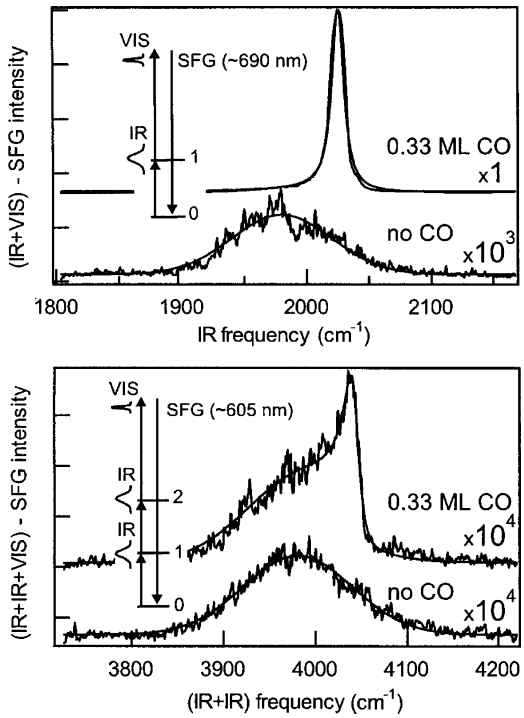

Figure 4. Upper panel: Conventional IR-visible SFG spectrum of the ν_1 mode of 0.33 ML CO on Ru(001) taken at 95 K, together with the nonresonant SFG signal from the bare surface. Lower panel: IR−IR−visible SFG spectrum from the same surface, as well as from the bare surface. The peak around 4040 cm^{-1} is assigned to two $n = 0 \rightarrow 1$ transitions. Reprinted with permission from ref 109. Copyright 2001 American Physical Society.

$\chi^{(3)}$. Namely, let $\langle n, m|$ be the stretching vibrational states of jth and kth CO. Then, one IR field resonantly excites the stretching mode of the jth CO, $\langle 0, 0| \rightarrow \langle 1, 0|$, and the second IR field excites the stretching mode of the kth CO, $\langle 1, 0| \rightarrow \langle 1, 1|$. The visible field with frequency ω_{VIS} then interacts to create a third-order nonlinear polarization at a frequency of $2 \times \omega_{01} + \omega_{VIS}$. The resonant part of $\chi^{(3)}$ is expressed as

$$\chi^{(3)} = \sum_{jk} (\partial^2 \alpha_g / \partial Q_j \partial Q_k)_0 (\partial \mu_g / \partial Q_j)_0 (\partial \mu_g / \partial Q_k)_0 \times \frac{\langle 0, 0|Q_j Q_k|1, 1\rangle\langle 1, 1|Q_j|0, 1\rangle\langle 0, 1|Q_k|1, 1\rangle}{(2\omega_{IR} - 2\omega_{01} + 2i\delta\omega_{01})(\omega_{IR} - \omega_{01} + i\delta\omega_{01})} \quad (60)$$

Here, Q_j is the vibrational coordinate of the jth molecule, and α_g is the collective polarizability of the system in the ground electronic state. Thus, $\chi^{(3)}$ is nonzero only if two different CO oscillators on the surface couple with each other via anharmonicity to affect the electronic polarizability. The term $(\partial^2 \alpha_g / \partial Q_j \partial Q_k)$ is proportional to r_{jk}^{-3}, where r_{jk} is the distance between the oscillators. Thus, the signal is dominated by neighboring CO adsorbates at short intermolecular distances.

Although this type of spectroscopy is very powerful for extracting interactions between adsorbates, applications to adsorbate systems are still scarce. Thus, it is highly desirable to develop 2-D spectroscopy on various adsorbate systems for a more detailed understanding of vibrational couplings among adsorbates.

6. Coherent Phonons at Semiconductor Surfaces and Buried Interfaces

Extensive studies have been done on coherent phonon generation and detection in bulk materials.[28,29,31,33,41,43,110−125]

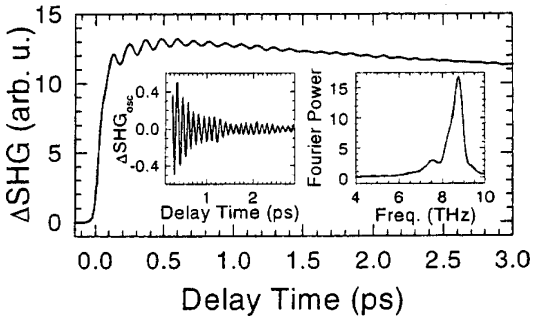

Figure 5. TRSHG trace from native-oxide-covered GaAs(100). Left inset: oscillatory part in the TRSHG trace. Right inset: Fourier power spectrum of the oscillatory part. The oscillatory modulations are due to local interfacial coherent phonon modes. Reprinted with permission from ref 36. Copyright 2000 Elsevier Ltd.

Readers interested in this subject should refer to the review of Dekorsy et al.[35] Usually, bulk coherent phonons are detected by time-resolved liner reflectivity. However, TRSHG has been used to monitor coherent phonons at surfaces and interfaces. The usefulness of this technique is because SHG is sensitive to those regions where inversion symmetry is broken as described in Section 4.1. This section describes coherent surface phonons at semiconductor surfaces and buried interfaces. In addition, we describe theoretical investigations on the flipping motion of Si dimers on Si(100).

6.1. GaAs Surfaces

TRSHG was first applied to GaAs surfaces by Tom and co-workers[55] and proved to be very versatile for the investigation of coherent motions of ions near the surface and interface regions. This method also has been applied to various GaAs surfaces in ultrahigh vacuum conditions, including GaAs(110)-(1 × 1), -(1 × 6), -(4 × 6) and -(4 × 1),[36,55,126] and GaAs(100)-c(8 × 2).[127]

Figure 5 shows a TRSHG trace taken from a native-oxide-covered GaAs(100) surface.[36] The oscillatory component is superimposed on the background signal with a steep rise and slow decay. The background signal originates from the carrier dynamics: the rapid rising edge is due to carrier injection and rapid carrier-induced screening of the depletion field in the bulk. The oscillatory part and its Fourier power spectrum are depicted in the left and right insets, respectively, and show the manifestation of a local interfacial coherent phonon mode. The peak is significantly reduced by Ar^+-ion sputtering and annealing, indicating that TRSHG is sensitive to the coherent phonon modes in a few monolayers of the surface. A similar surface sensitivity also has been demonstrated for GaAs(100)-c(8 × 2).[127]

As pointed out in Section 3.5, the excitation mechanism for coherent phonons observed on those semiconductor surfaces is attributed to DECP associated with carrier-induced screening of the depletion field. In fact, the Fourier power spectrum of the oscillatory part in a TRSHG signal depends on pump fluence, i.e., the injected carrier density. The oscillatory part can be decomposed into three components: 8.80 (293 cm^{-1}), ~7.6 (250 cm^{-1}), and ~8.4 THz (280 cm^{-1}). The 8.80-THz (293 cm^{-1}) mode is the well-known bulk LO phonon mode at the Γ point. Since GaAs crystals lack inversion symmetry in the bulk, SHG is not confined at their surfaces. In this study, 850 and 425 nm radiation are used as the fundamental and second-harmonic, respectively. Thus, the experiments are sensitive to the 15-nm-thick topmost layer, mainly determined by the optical

attenuation of 425 nm light in the bulk. The intensity of the ~7.6-THz (250 cm^{-1}) mode increases with injected carrier density, which is consistent with the LO-phonon−electron-plasmon coupled mode.[128] The mode at ~8.4 THz (280 cm^{-1}) is assigned to a local interfacial mode confined to a few monolayers of the interface.

This method provides a way of monitoring modifications to the surface due to adsorbates. Tom and co-workers[36,126] have investigated spectral changes upon oxygen exposure. As a clean surface is exposed to oxygen, the 8.2-THz (270 cm^{-1}) mode grows, while the other modes remain constant. Thus, this mode is characteristic of clean and oxidized layers. The progression of Fourier power spectra obtained from TRSHG traces as a function of oxygen exposure indicates that this method has submonolayer sensitivity to chemical and structural changes associated with adsorbates.

Chang et al.[129] investigated coherent phonons near the surface region of InN by TRSHG. A coherent phonon mode at 13.4 THz (447 cm^{-1}) was assigned to the longitudinal optical phonon and plasmon coupling mode. The coherent phonon shows cosine-like behavior, indicating that it is driven by a displacive force. The phonon amplitude was measured as a function of the angle ϕ of the polarization of the pump pulses with respect to the crystal axis. If the coherent phonon is excited by the ISRS process, the phonon amplitude is expected to show angular dependence $A \sin(2\phi) + B$, where A and B are constants. However, the phonon amplitudes do not depend on ϕ. Thus, the excitation of the coherent phonon is dominated by DECP associated with transient electric field screening.

6.2. Buried Interfaces in Semiconductors

Recently, TRSHG has been applied to buried interfaces of GaP Schottky diodes,[130] and GaInP/GaAs/GaInP single quantum wells.[131] In GaP Schottky diodes, a coherent longitudinal acoustic phonon (122 GHz, 4.07 cm^{-1}) was observed in addition to a coherent longitudinal optical phonon (12.2 THz, 407 cm^{-1}) in the near surface region of GaP. The coherent acoustic phonon is created at the metal−semiconductor interface by transient thermal strain. The pump power and polarization dependence of the optical phonon were measured. If displacive excitation by photoexcited carriers is responsible for the coherent optical phonon, the phonon amplitude should increase quadratically with pump power, since carriers are created by the two-photon process with a pump pulse of 1.56 eV. However, the phonon amplitude increases linearly with pump power, which excludes displacive excitation by photoexcited carriers. The phonon amplitudes clearly depend on the angle of pump polarization with respect to the crystal axis. From an analysis of the polarization dependence, it was concluded that ISRS and DECP associated with transient electric-field screening are responsible for creating the optical phonon.

Coherent phonon modes of GaInP/GaAs/GaInP single quantum wells[131] were also investigated by TRSHG, together with spontaneous Raman scattering and time-resolved reflectivity change measurements. Figure 6 shows a typical TRSHG trace and the spectra obtained from this trace. Six phonon modes are assigned to GaP-like LO phonons at ~11.5 THz (384 cm^{-1}), InP-like LO phonons at ~10.7 THz (357 cm^{-1}), an LO-plasmon coupling mode in the InGaP barrier at 10.0 THz (334 cm^{-1}), interfacial phonons in the GaAs/GaInP hetero-interface at 9.4 THz (310 cm^{-1}), LO phonons in the GaAs well at ~8.8 THz (290 cm^{-1}), and an

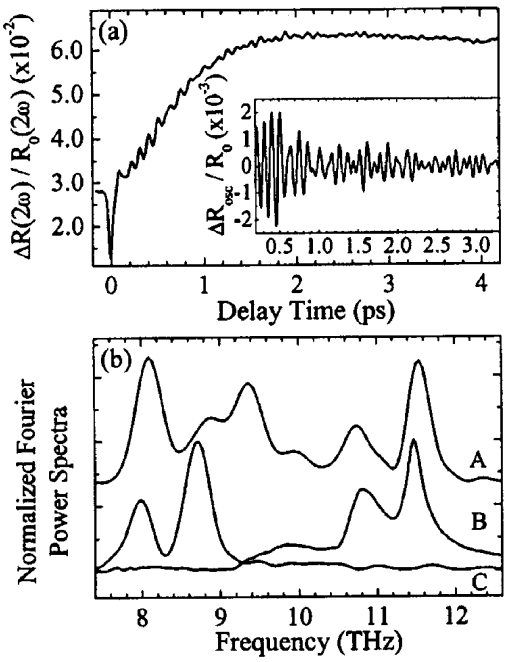

Figure 6. (a) TRSHG trace of a GaInP/GaAs/GaInP single quantum well. The oscillatory component is shown in the inset. (b) Fourier power spectrum of the oscillatory component of TRSHG trace (curve A), spontaneous Raman scattering spectrum (curve B), and spectrum from time-resolved reflectivity change measurements (curve C). Reprinted with permission from ref 131. Copyright 2004 American Institute of Physics.

LO-plasmon coupling mode in the GaAs buffer layer at ~8.0 THz (270 cm^{-1}). These assignments are based on the fact that transient reflectivity change provides information on bulk phonons, while spontaneous Raman scattering only gives Raman-active modes. The peak at 9.4 THz (310 cm^{-1}) appears clearly in the TRSHG spectrum and slightly on the shoulder in the Raman spectra and is attributed to a phonon mode at the interface of GaAs/GaInP in the quantum wells.

6.3. Buckled Silicon Dimers on Si(100)

Silicon is a basic material for electronic device technology. As miniaturization of electronic devices proceeds, coupling of electrons and phonons in addition to electron−electron scattering at surfaces and interfaces increasingly determines device performance. In this context, coherent surface phonon dynamics are useful to explore the electron−phonon coupling at silicon surfaces. Carrier dynamics at various semiconductor surfaces was reviewed by Haight[132] and more specifically those at a Si(100) surface have been investigated recently by time-resolved 2PPE[133] and five-wave-mixing spectroscopy.[134] Moreover, generation of bulk coherent phonons and subsequent dressing of the phonons by electron−hole pair excitations have been investigated by time-resolved reflectivity measurements with 10-fs laser pulses.[135]

A Si(100) surface has characteristic buckled Si dimers as a result of surface reconstruction. The origin of the buckled dimers is understood by rehybridization of the orbitals of Si dimers. The dangling bonds rehybridize into an unoccupied *p*-like orbital and an occupied dangling-bond orbital with a somewhat larger *s*-character. This can be viewed as symmetry breaking by a Jahn-Teller effect. This reconstruction leads to changes in the band structure of the Si(100) surface from metallic to semiconducting.

When an electronic transition between the occupied and the unoccupied states of dimers takes place, the buckled Si

dimer structure is expected to be modified. If half of the electrons in the occupied band were excited into the unoccupied band, the dimer structure would be changed from a buckled configuration to a symmetric one. Even in weaker excitations, the vibrational motion of the buckled dimer would be excited. Unfortunately, no experimental results have been reported on coherent vibrational excitation of Si dimers by ultrafast laser irradiation; it has only been studied theoretically.[136]

The calculations are based on time-dependent density functional theory combined with Ehrenfest dynamics for nuclear motion. The dynamics of a Si dimer was simulated when the surface is excited by a 25-fs Gaussian-shaped laser pulse. The dimer starts oscillating by changing the buckled angle from 19° to 5° associated with the change of the dimer bond length. During the first 250 fs, the kinetic energy is preferentially concentrated in the dimer oscillating motion. Although the buckled dimer structure is not completely flipped, this simulation indicates that electronic excitation of the dangling-bond states with short laser pulses induces vibration of the buckled dimer. The total energy deposited in the supercell amounts to 16 eV, corresponding to 0.7 eV per Si atom. The threshold fluence for ablation of silicon[137] is 0.52 J cm^{-2} i.e., $\sim 6 \times 10^{-5}$ eV per atom, which is far below the cohesive energy of bulk silicon. Thus, although this molecular dynamics simulation suggests that the excitation of the vibration of buckled dimers on Si(100) is feasible by laser pulses with a duration of 25 fs, it is difficult to realize this without ablation of surface atoms.

7. Coherent Phonons of Adsorbate–Substrate Modes on Metal Surfaces

Alkali-metal atoms on metal surfaces are one of the simplest chemisorbed systems and are useful for many applications, including promotion of catalytic reactions[138−140] and enhancement of electron emission.[141−143] The electronic structure of alkali adsorbates on metal surfaces strongly depends on the alkali coverage. Thus, alkali-atom adsorption systems provide a good opportunity to investigate how coherent motions of alkali atoms are created and evolve under very different electronic configurations. Coherent motions of alkali atoms have been recently investigated in two different coverage regimes. For the low coverage regime, Petek and co-workers have investigated coherent wave packet motion in alkali-atom-induced electronically excited states by interferometric time-resolved two-photon photoemission (ITR-2PPE).[13,144−146] For the high coverage regime, Matsumoto and co-workers have investigated coherent vibration of the stretching mode of alkali atoms by TRSHG.[9,14,147−149] In this section, we describe coherent motions at metal surfaces induced by femtosecond-laser irradiation.

7.1. Geometric and Electronic Structures of Alkali-Atom Adsorbates on Metal Surfaces

The geometric and electronic structures of alkali atoms on metal surfaces have been extensively studied, and many reviews[139,150−153] have been written on this subject. Alkali-atom adsorbates show a variety of adsorption structures on metal surfaces, depending on the combination of alkali atom and metal substrate, the alkali atom coverage, and the surface temperature. These structures have been reviewed comprehensively by Diehl and McGrath.[153] Tochihara and co-workers[154−156] have conducted detailed studies on the complicated

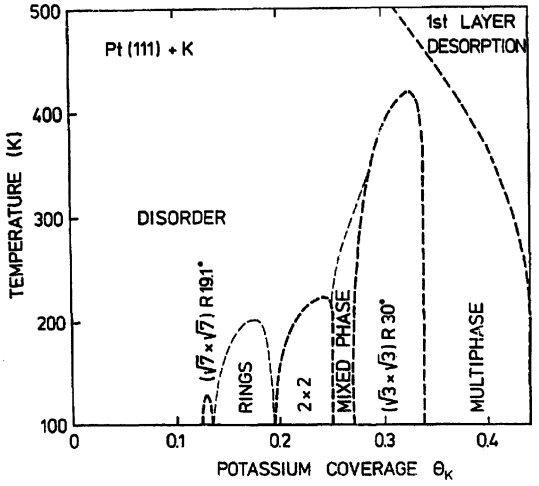

Figure 7. Approximate phase diagram of K on Pt(111) observed by LEED. Reprinted with permission from ref 157. Copyright 1988 Elsevier Ltd.

structural changes of Li-covered Cu(001) and Cu(110) surfaces as a function of coverage by low-energy electron diffraction (LEED) and scanning tunneling microscopy (STM). Since we only discuss alkali adsorption systems on flat (111) surfaces, we briefly describe the geometric structures of K on Pt(111) as a representative example.

Figure 7 shows a phase diagram of K adsorption on Pt-(111) obtained from LEED pattern observations.[157] Below $T \sim 200$ K, for which coherent surface phonon measurements described in Section 7.3 have been conducted, K adsorbates show distinct superstructures, depending on the coverage. In the narrow coverage range around $\theta = 0.14$ ML, the $(\sqrt{7} \times \sqrt{7})R19.1°$ structure appears. In the coverage range $0.2 < \theta < 0.4$ ML, the LEED pattern changes to diffraction rings, indicating a reasonably well-defined nearest-neighbor distance but no long-range rotational correlations in these dispersed overlayers. As the coverage increases, hexagonal superstructures appear, including (2×2) and $(\sqrt{3} \times \sqrt{3})R30°$. As discussed later, the formation of the superstructures allows the observation of coherent surface phonon modes of the metal substrate in addition to the stretching mode of alkali atoms with respect to the metal surface.

Knowledge of the electronic structure of alkali-atom-covered metal surfaces is vital for clarifying the excitation mechanism for coherent motions under femtosecond-laser pulse irradiation. It is well-known that the work function of metals is greatly affected by alkali-atom adsorption. The work function of a bare metal surface decreases significantly at low coverages. As the coverage increases, the work function increases slightly and levels off eventually at higher coverages. The traditional explanation of this behavior was given by Gurney.[158] In this picture, partial *s*-electron donation takes place from alkali atoms to the metal surface at low coverages and thereby the bonding of the alkali atom with the metal becomes ionic. This makes a large dipole layer responsible for the significant decrease in the work function. As the coverage increases, repulsive dipole−dipole interactions become prominent and mutual depolarization of the dipoles decreases the net charge of the charge-transfer per adatom. At high coverages, the orbital overlap of the alkali atoms is large enough that the alkali overlayer becomes metallic. On the other hand, a covalent picture has been proposed, in which significant charge redistribution takes place within the alkali atoms to form dipoles.[159] In this

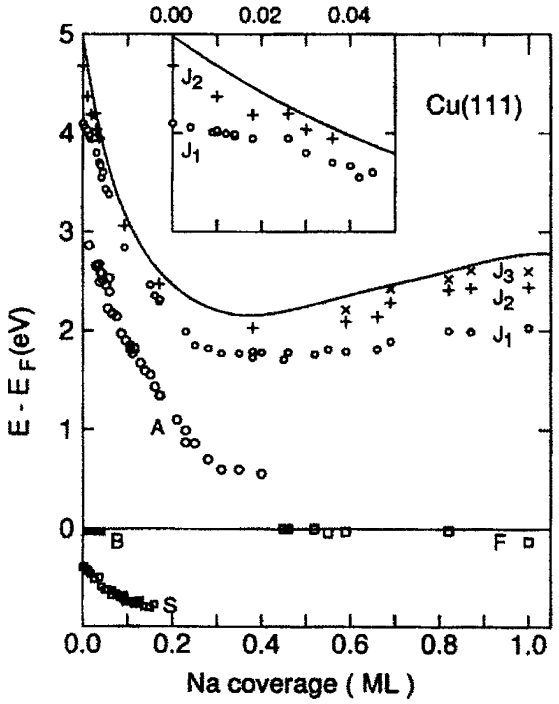

Figure 8. Energy levels of a Na-covered Cu(111) surface as a function of Na coverage observed by 2PPE. The coverage denoted here is normalized by the saturation coverage of 4/9 ML. The vacuum level is indicated by the solid line. The inset shows the region of small coverage. Reprinted with permission from ref 161. Copyright 1994 Elsevier Ltd.

picture, the net charge of the alkali atoms does not change with coverage. Although these pictures are apparently very different, the determination of the net charge of the alkali atoms is somewhat arbitrary. Thus, it appears that the distinction between the two pictures of charge redistribution is rather semantic.

Fischer et al.[160,161] studied the electronic structure of Na on Cu(111) as a function of Na coverage by 2PPE, as shown in Figure 8. At saturation coverage, the Na overlayer has a hexagonal ($3/2 \times 3/2$) structure, corresponding to a coverage of $\theta = 4/9 \approx 0.44$ ML.[162] Note that the coverages shown in Figure 8 are normalized by the saturation coverage. A series of unoccupied states near the vacuum level follow the work function changes.[161] Furthermore, an adsorbate-induced state was also identified in the 2PPE measurements. While the adsorbate-induced state is unoccupied at low coverages, this state is stabilized and located below E_F at high coverages. Thus, the 2PPE studies clearly show that the bonding nature changes with coverage. In the following subsections, we describe the electronic structure and coherent nuclear motions created by femtosecond-laser-pulse irradiation in the two coverage regimes.

7.2. Ultrafast Nuclear Dynamics at Low Coverages

Petek and co-workers have investigated the wave packet motion of Cs on a potential energy surface associated with the transition from the occupied surface state to the Cs-induced excited surface state using ITR-2PPE spectroscopy.[13,144−146] The electronic structure of Cs-covered Cu(111) at low coverage was first characterized by 2PPE. On a clean Cu(111) surface, an occupied Shockley-type surface state (SS) exists at 0.39 eV below E_F. When Cs is adsorbed on this surface, a new resonance peak appears in the 2PPE

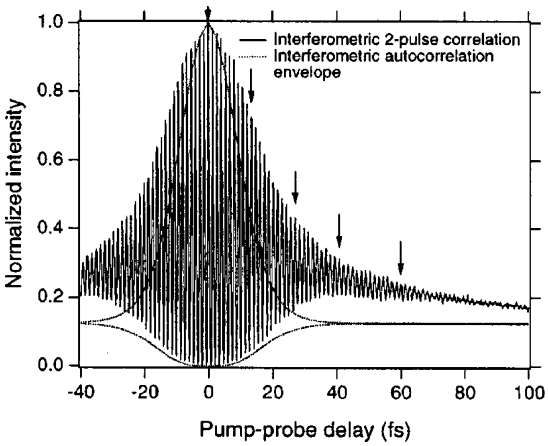

Figure 9. Interferometric two-pulse correlation scan taken from Cs/Cu(111). The signal was measured for the intermediate state energy of 2.52 eV. The deviation from the envelope of the interferometric autocorrelation is due to the finite phase and energy relaxation rates. Reprinted with permission from ref 13. Copyright 2000 American Chemical Society.

spectra. This resonance is attributed to the transition from the surface state to the antibonding unoccupied state (A) as found in the case of Na on Cu(111).[160,161]

ITR-2PPE provides both the population decay and dephasing time of electronic coherent polarization created by a pump pulse. Two femtosecond pulses, the pump and probe, whose optical phases are locked, are irradiated onto the Cu(111) surface covered with Cs. The pump pulse with photon energy resonant with the SS → A transition creates coherent polarization. A delayed probe pulse interacts with the created coherent polarization of the system. Figure 9 shows a typical interferometric two-pulse correlation trace. When the photon energy is off-resonant, the excited state is virtual, so that an ITR-2PPE trace just shows the interference patten of the two pulses. On the other hand, an ITR-2PPE trace for resonant excitation is broader than the autocorrelation trace, revealing the phase relaxation of the created coherent polarization and the population decay of the A state.

The ITR-2PPE traces are simulated by an optical Bloch equation formalism which describes the optical coupling of multiple electronic states. The optical Bloch equations of a three-level system consisting of SS, A, and the detected portion of the final state free-electron wave continuum are solved for the time-integrated population of the final state as a function of pump−probe delay.[144,163] Parameters involved in the simulations are the energy levels of the electronic states, the laser detuning energy with respect to each optical transition, and the phase and energy relaxation times. The simulations of ITR-2PPE traces gives a phase relaxation time of 15 fs and population decay time of 50 fs at a surface temperature of 33 K,[144,145] which is substantially longer than the population decay time of 15 fs at 300 K reported earlier.[164,165]

The long population decay time of the antibonding state is due to a barrier for electron decay into the bulk because the A state is in the *s*, *p*-inverted band gap at the $\bar{\Gamma}$ point. In fact, the lifetime of the A state is significantly shorter on Cu(110), which does not have a band gap at the $\bar{\Gamma}$ point. Borisov et al.[166,167] calculated the lifetime of the A state theoretically using the coupled angular mode and wave packet propagation methods, showing that the lifetime is longer than that calculated for free-electron metal surfaces. Thus, the Cu(111) projected band gap along the normal to

the surface causes a barrier for resonant electron transfer from the A state to bulk bands.

An intra-atomic hybridization model is useful for understanding the nuclear dynamics associated with the electronic transitions of the alkali-atom adsorption system in the low coverage regime.[168,166] In this model, when Cs approaches the metal surface, the 6s and 6p orbitals of Cs are strongly hybridized, resulting in two hybridized orbitals: $|6s + 6p_z\rangle$ and $|6s - 6p_z\rangle$. The electron density is concentrated at the vacuum side for the former orbital and at the surface side for the latter with respect to the Cs atom. Thus, the upper $|6s + 6p_z\rangle$ state is antibonding, whereas the lower $|6s - 6p_z\rangle$ state has a bonding nature. Thus, excitation to the antibonding state by an ultrafast laser pulse significantly weakens the Cs−Cu bond, so that a nuclear wave packet associated with femtosecond-pulse excitation is created on the repulsive potential energy surface of the excited state.

When the photon energy is tuned to the resonance transition of SS → A, the two-pulse correlation consists of a fast decay of the coherent polarization and a slower, strongly energy-dependent, nonexponential decay. This nonexponential decay corresponds to the antibonding state population dynamics. This feature is attributed to the desorptive motion of Cs atoms. The 2PPE spectra become broader and shift to lower energy over the delay time due to the evolution of the wave packet of Cs on the excited-state potential energy surface (see Section 9.1). The observed results provide information on the slope of the excited-state potential energy surface in the vicinity of the ground-state equilibrium distance. Although the adsorbate system is excited to the repulsive antibonding state, the photodesorption cross section is estimated to be very low, i.e., $\leq 2.4 \times 10^{-23}$ cm^2. This contrasts sharply with the desorption cross section of K from a graphite surface,[169] 1.8×10^{-20} cm^2. The difference may arise from both different potential energy surface topologies and nuclear masses. The extremely small desorption cross section for Cs/Cu(111) indicates that the slope of the excited potential energy surface is not steep enough, so that a Cs atom cannot gain enough kinetic energy for desorption before the excited state is quenched back to the ground state. In addition, the recoil motion of lighter Cu atoms pushed by the heavy Cs atom may also be responsible for the small cross section.[8,145] Thus, at this end, most of the excited Cs atoms are quenched in the deep adsorption well and likely vibrate coherently. Indeed, coherent vibration of alkali atoms in the adsorption well has been observed, as described in the next subsection.

7.3. Coherent Vibrations in High Coverages

7.3.1. Metallic Quantum Well States

When the coverage of alkali atoms increases, the electronic structure and bonding nature change dramatically. At high coverages, the overlayer of alkali atoms forms a metallic quantum well confined between the vacuum barrier and the metal substrate. The quantum well states of Na on Cu(111) have been investigated by inverse photoemission spectroscopy (IPES),[170] 2PPE,[160,161] and scanning tunneling spectroscopy (STS).[171−174] As shown in Figure 8 the alkali-induced state decreases in energy with an increase in Na coverage and crosses E_F at $\theta \approx 0.35$ ML. In contrast to the alkali-induced state, unoccupied image states follow the vacuum level. Carlsson et al.[175] studied in detail the occupied quantum well state by high-resolution photoemission as a function of Na coverage. The occupied and unoccupied states of Na on Cu(111) have also been observed by STS.[171] At $\theta = 0.27$ ML, the derivative of the tunneling current dI/dV as a function of bias voltage clearly shows that the quantum well states are located at $E_1 \sim 0.4$, $E_2 \sim 2.0$, and $E_3 \sim 2.9$ eV above E_F. In addition, photon emission at $h\nu = 1.7$ eV was observed when the sample bias was adjusted such that an electron was injected into the upper quantum well state at $E_2 \sim 2.0$ eV. The emitted photon energy is consistent with the energy of the interband transition from E_2 to E_1.[176]

Energy dispersion along the parallel momentum of the lower quantum well state was measured by IPES[170] and 2PPE.[160] The IPES spectrum at a coverage of 0.25 ML showed that the unoccupied state at 0.4 eV exhibits a nearly-free-electron-like feature. By angle-resolved 2PPE, the effective electron mass in the occupied state was evaluated to be 1.3 ± 0.1 at saturation coverage of 0.44 ML.

Carlsson and Hellsing[176] performed first-principles calculations of the electronic states of Na on Cu(111) in two different adsorbate structures: (2×2) and $(3/2 \times 3/2)$. They found that Na-induced bands are located at 0.45 and 2.36 eV above E_F for (2×2) and 0.06 eV below E_F for $(3/2 \times 3/2)$. In fact, the two Na-induced bands for (2×2) were confirmed later by the STS measurements.[171] The local density of states of the occupied state at $\bar{\Gamma}$ has a maximum in the interfacial region between the Na overlayer and the vacuum barrier and a smaller maximum at the interface between the overlayer and the substrate. As expected, this amplitude decays rapidly into the substrate. In addition, the dispersion of the band along the surface plane, i.e., $\bar{K} - \bar{\Gamma} - \bar{M}$ is in good agreement with that determined by 2PPE.[160] Thus, the experimental and theoretical studies have established a very firm basis of the metallic quantum well states of Na overlayers on Cu(111). A metallic quantum well should also be formed for other combinations of alkali-atom and metal substrate.

7.3.2. Coherent Surface Phonons

Here we describe the coherent oscillation mode of alkali atoms induced by excitation between metallic quantum well states. When a Pt(111) surface covered with 0.25 ML Cs is irradiated by 150-fs laser pulses at 800 nm, Watanabe et al.[147] have found by TRSHG measurements that coherent vibration of the Cs−Pt stretching mode is generated. Figure 10 shows TRSHG traces taken from clean and Cs-covered Pt(111) surfaces. The TRSHG trace from the clean surface shows an instantaneous sharp rise immediately after the excitation. This is followed by a rapid decaying component ($t_d < 1$ ps) and a slowly decaying one ($t_d > 1$ ps). The TRSHG trace shows a very similar temporal response of the transient temperature of electrons. Thus, hot electrons generated by a pump pulse give major contributions to the TRSHG signals at a clean surface.

When the Cs coverage is increased, the second harmonic intensity is strongly enhanced by adsorption of Cs compared with the clean surface. More importantly, clear oscillatory signals appear in TRSHG traces after the strong peak at $t = 0$. The oscillatory part is well fitted by a single underdamped oscillator with a frequency of 2.30 THz (76.7 cm^{-1}) and a damping constant of 1.39 ps. The frequency of the oscillatory signal is close to those of the Cs-substrate stretching vibrational mode of Cs/Cu(100) (55 cm^{-1})[177] and Cs/Ru(0001) (54−72 cm^{-1}).[178] When Cs is replaced by K, the frequency of the oscillating mode is 4.7 THz (157 cm^{-1}) at

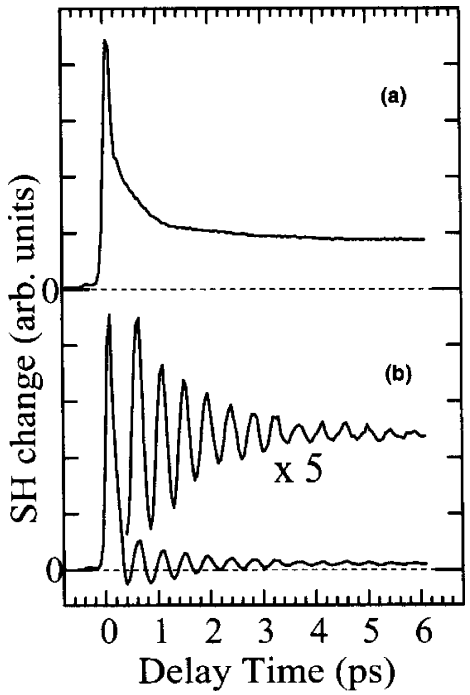

Figure 10. TRSHG traces taken from (a) clean and (b) 0.25 ML Cs covered Pt(111) surfaces. A clear oscillatory component of 2.3 THz is seen in (b). The vertical scales are normalized at each peak of the TRSHG trace. Reprinted with permission from ref 147. Copyright 2002 Elsevier Ltd.

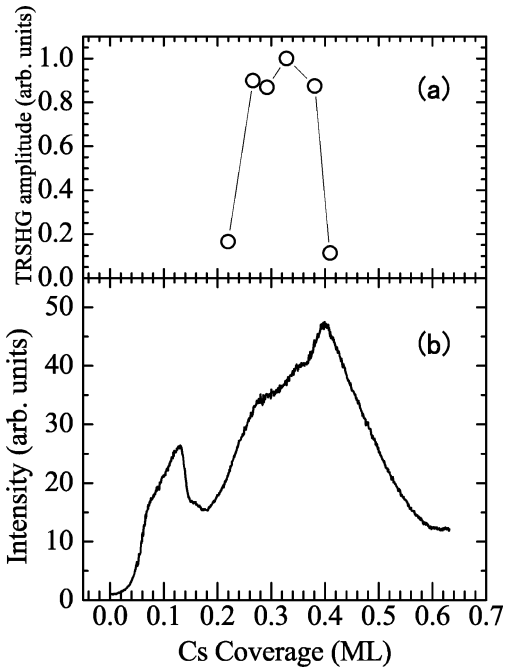

Figure 11. (a) Amplitude of the oscillating component in TRSHG traces and (b) relative second harmonic intensity of 800-nm probe pulses, measured for Cs/Pt(111), plotted as a function of Cs coverage. The Cs coverage was defined by referencing to atom density of the metal substrate. The first layer is completed at 0.41 ML (1 ML = 1.5×10^{15} cm^{-2}).

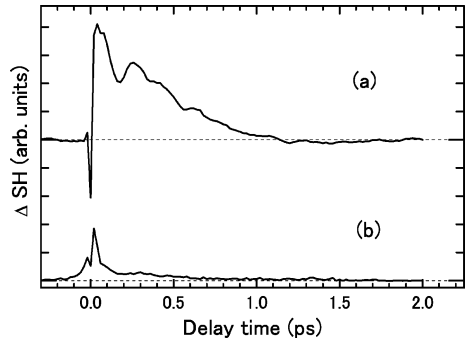

Figure 12. Photon energy dependence of TRSHG traces taken from a Na-covered Cu(111) surface. The Na coverage is the full coverage of 0.44 ML. The pump photon energy was tuned to (a) 2.1 and (b) 2.0 eV, while the photon energy of the probe pulses was fixed at 2.1 eV.

0.32 ML, which is also in good agreement with that of the K−Pt stretching vibrational mode measured by HREELS.[179] Thus, these oscillating signals in TRSHG traces are attributed to coherent vibrations of the alkali atom-Pt stretching mode.

7.3.3. Excitation Mechanism

As described in Section 4.3, a strong second harmonic intensity of probe pulses is necessary to recover oscillating signals due to nuclear coherent motions in TRSHG measurements with reasonable signal-to-noise ratios, since this technique relies on heterodyne detection. Alkali-atom-covered metal surfaces satisfy this condition. Figure 11 shows variations in the second harmonic intensity of probe pulses at 800 nm for Cs on Pt(111), exhibiting peaks at $\theta = 0.12$ and 0.4 ML. The second harmonic intensity increases by almost 2 orders of magnitude when Cs is adsorbed. These remarkable enhancements in second harmonic intensity are commonly observed for alkali-metal adsorption systems on metal surfaces. The origins of the enhancement are attributed to the local-field enhancement at the adsorbate−vacuum interface and/or interband transitions between two-dimensional alkali-metal adsorbate induced states.[180,181]

The initial modulation amplitudes of TRSHG traces are also plotted in Figure 11. Note that the variations in second harmonic intensity are not necessary correlated to the modulation amplitudes in TRSHG traces. Thus, not all electronic resonance transitions that enhance second harmonic intensity are relevant to the creation of coherent vibration.

Although Cs adsorbates can create a metallic quantum well at the Pt(111) surface similar to Na on Cu(111), the precise energies of quantum well states are not known. Thus, we have studied the excitation photon-energy dependence of the oscillation amplitudes for Na/Cu(111) at the full Na coverage (0.44 ML), since the electronic structure of Na/Cu(111) is well characterized as described in the previous subsection (see Figure 8). TRSHG traces were measured at the photon energy of the pump pulses at 2.0 and 2.1 eV, while that of the probe pulses was fixed at 2.1 eV. At 2.0 eV, no oscillatory signals were observed in the TRSHG trace, as shown in Figure 12. When the excitation energy was tuned to 2.1 eV, an oscillatory component due to coherent vibration of the Na−Cu stretching mode at 5.4 THz (180 cm^{-1}) was clearly observed.

Resonant ISRS is a possible excitation mechanism for the coherent oscillation of Na, since a photon energy of 2.1 eV is resonant to the transition from the adsorbate-induced quantum-well state at 0.4 eV below E_F to the first image state. The excited-state relevant to the resonant transition is composed of an electron in the image state and a hole in the adsorbate-induced occupied state. Since the adsorbate-induced occupied state is most responsible for the bonding of Na to the Cu substrate, the involvement of the excited

state in the transition is very effective to make vibrational coherence with respect to the Na−Cu stretching mode.

Creation of holes in the adsorbate-induced occupied state also can be achieved by optical transitions other than the resonant transition discussed in the last paragraph. Absorbance of bulk Cu substantially increases when the photon energy changes from 2.0 to 2.1 eV, because the transitions from the Cu *d*-bands to empty bands right above E_F become significant at 2.1 eV. Holes created in the *d*-bands by the optical transitions could be filled by electrons in the adsorbate-induced occupied state of the metallic quantum well by an Auger-type transition. Hence, holes can be created in the adsorbate-induced occupied state. Moreover, since this Auger decay can occur significantly faster than the oscillation period of the Na−Cu stretching mode, the substrate excitation may also be a possible excitation mechanism for the coherent oscillation.

In either case, a displacive force is exerted to Na−Cu oscillators, leading a cosine-like oscillation. In fact, the oscillating components observed in the TRSHG traces are all cosine-like. More detailed measurements of excitation photon energy dependence are needed for a clear understanding of the excitation mechanism.

7.3.4. Dephasing

Here we describe dephasing of the coherent vibration of the alkali-atom stretching mode. As described in Section 5.2, the dephasing rate of coherent vibrations on a metal surface is given by

$$\gamma = 1/T_2 = \gamma_{eh} + \gamma_{ph} + \gamma_{dep} \tag{61}$$

where γ_{eh} and γ_{ph} are the dephasing rates by substrate electron−hole pair excitation and by direct coupling to substrate phonons, respectively, and γ_{dep} is the pure dephasing rate due to anharmonic coupling to low-frequency lateral modes or substrate phonon modes.

The γ_{eh} contribution to the total dephasing rate should be substantial, since alkali-atoms interact strongly with metal substrates. Since the frequencies of the alkali-atom stretching modes are below the maximum phonon frequencies of bulk Pt and Cu, the contribution of γ_{ph} to the total dephasing rate should also be substantial. Since these dephasing rates are insensitive to surface temperature as long as the vibrational mode can be treated as a harmonic oscillator,[77] the dephasing rate of the alkali-atom stretching mode should not strongly depend on surface temperature, unless pure dephasing is effective.

Watanabe et al.[9] found that the frequency and dephasing rate of the Cs−Pt stretching mode strongly depend on surface temperature. As the temperature increases, the frequency decreases and the dephasing rate increases. Therefore, although electron−hole pair creation and phonon emission contribute to the vibrational relaxation, pure dephasing plays an important role in the dephasing process.

As in the case of CO on metal surfaces described in Section 5.2.2, Watanabe et al. examined whether the variations in the central frequency and dephasing rate can be interpreted by hot bands as the temperature increases. When a Morse potential function is adapted along a Cs−Pt coordinate, the transition energy between the adjacent vibrational levels is given by

$$\Delta E_v = \hbar\omega_0[1 - 2\chi_e(\upsilon + 4)] \tag{62}$$

where χ_e is an anharmonic coupling parameter and υ is a vibrational quantum number. As the temperature increases, transitions from higher vibrational states contribute to the spectra, resulting in a mean transition energy of

$$\Delta E(T) = \frac{\sum_\upsilon \Delta E_\upsilon e^{-E(\upsilon)/kT}}{\sum_\upsilon e^{-E(\upsilon)/kT}} \tag{63}$$

Under the assumption that all the contributions to the vibrational coherence from the higher vibrational quantum numbers overlap in-phase in TRSHG signals and that the vibrational dephasing rate is independent of υ, the observed peak shifts are well reproduced by eq 63 with an anharmonicity parameter of $\chi_e = 0.0054 \pm 0.0006$ and $\omega_0 = 2.32 \pm 0.01$ THz. However, the dephasing rate cannot be reproduced with the same χ_e. Thus, the temperature dependence of the dephasing rate cannot be interpreted by a simple model that only takes into account the anharmonic shift in the Cs−Pt vibrational frequency.

The frequencies of parallel modes in a Cs adlayer on Cu(001) have also been determined for 0−5 meV (0−40 cm^{-1}) by helium atom scattering.[177] The parallel modes of Cs on Pt(111) likely fall in a similar frequency range. Since the frequencies are very low, they are populated thermally. Thus, anharmonic coupling between the Cs−Pt stretching mode and parallel modes enhances the dephasing rate as the temperature increases. This pure dephasing is likely to be the dominant mechanism of the temperature dependence of the dephasing rate.

Vibrational relaxation at surfaces has been studied theoretically for adsorbates such as carbon monoxide[74] and hydrogen[20,182] interacting strongly with various metals. The theory accounts for the experimentally observed relaxation rates of vibrational modes of the adsorbates whose frequencies are higher than those of bulk phonon modes. The theory has been extended to apply to the low-frequency modes of adsorbates, where the resonance frequencies of the adsorbate modes are below the highest phonon frequency of the substrate.[183] The theoretical estimates are in reasonable agreement with observed values for adsorbates interacting weakly with metal substrates such as saturated hydrocarbons on metals. However, it has been tested only for weakly interacting systems, not for strongly interacting adsorption systems. Thus, it is desirable that the theory be tested for vibrational modes of adsorbates strongly interacting with substrates, as in the case of alkali-atoms on metal substrates, whose frequencies are in resonance with bulk phonons.

7.3.5. Effect of Substrate Electronic Excitation

As the fluence of the pump pulses increases, substantial electron−hole excitations take place in the metal substrate in addition to resonant excitation between the metallic quantum-well states. Femtosecond-laser pulse irradiation creates nonthermalized electrons. The maximum electron temperature of the substrate is rapidly established after thermalization by electron−electron scattering. This thermalization takes place usually within the femtosecond-laser pulse owing to effective electron−electron scattering. Because of the small heat capacity of the electrons, the maximum electron temperature can be far above the melting point of the substrate lattice. Then, it decays with a time

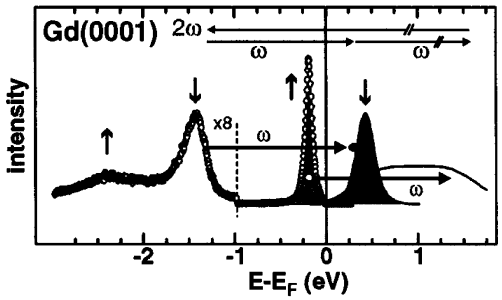

Figure 13. Electronic structure of Gd(0001). The occupied bands are observed by photoemission and the unoccupied bands are observed by inverse photoemission and scanning tunneling spectroscopy. Indicated are the two main absorption channels for 1.52-eV pump photons (ω) and the second harmonic probing scheme (2ω). Reprinted with permission from ref 185. Copyright 2003 American Physics Society.

constant of ~1 ps after the pump pulse as a result of electron−phonon coupling. Since the dephasing times of the coherent vibrations of alkali-atoms are in the range of 1−2 ps, the coherent vibrations dephase while the electron temperature in the substrate is very high.

The pump−fluence dependence of alkali-atom coherent vibration has been measured for Cs on Pt(111).[148] As the fluence increases, the initial modulation amplitude of the oscillating signals in the TRSHG traces increases, and a fast dephasing component becomes appreciable. This component has a dephasing time of 0.7 ps, and its center frequency is redshifted by ~0.1 THz from that obtained at low fluence. The initial amplitude of the fast component increases nonlinearly with the fluence. Since the electron temperature is greatly raised in the time domain where the fast component dominates, the fast component likely originates in interactions of hot electrons with adsorbates. As in the case of CO on metals described in Section 5.2.2, hot electrons may couple effectively with the lateral modes of alkali-atom adsorbates. Since excitation of the lateral mode is expected to be due to electron friction, this coupling should nonlinearly increase with the hot electron temperature. This accords with the observed result that the amplitude of the fast dephasing component increases nonlinearly with the fluence of the pump pulse. Thus, the pump−fluence dependence of the dephasing of the Cs-stretching mode can be understood as being pure dephasing induced by coupling to the lateral modes.

8. Coherent Phonons at Ultrathin Metal Film Surfaces

In the previous sections, we described the generation of coherent surface phonons by femtosecond-laser pulses and their dephasing processes. In this section, we review studies on the coupling of coherent phonons to spin dynamics at the surface of ferromagnetic Gd(0001). In addition to semiconductor surfaces (Section 6) and alkali-atom-covered metal surfaces (Section 7), TRSHG is also a versatile method for ferromagnetic Gd(0001) surfaces. These studies demonstrate that coherent phonons can be used to drive the spin system in the THz regime.

8.1. Coherent Surface Phonons and Coupling with Magnons

The electronic structure of Gd(0001) is depicted in Figure 13. A $5d_z^2$ surface state of Gd(0001) is exchange split into

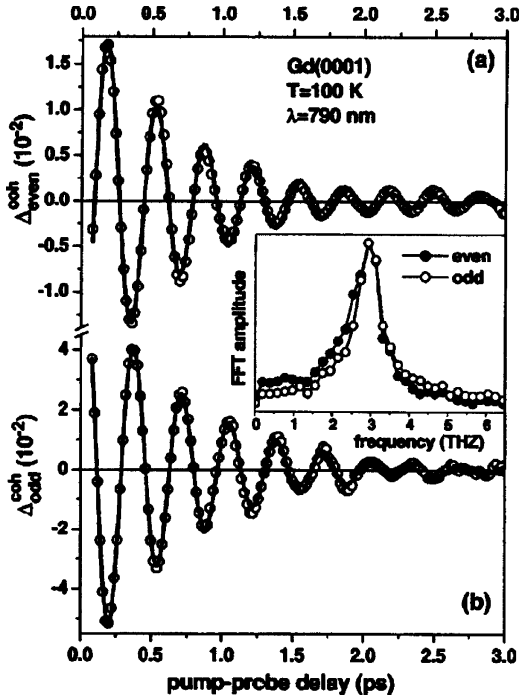

Figure 14. Coherent (a) even and (b) odd second harmonic fields obtained from TRSHG measurements. Incoherent background signals are subtracted. The inset displays the Fourier transform of the oscillatory signals. Reprinted with permission from ref 186. Copyright 2005 Optical Society of America.

an occupied majority (spin-up) and an unoccupied minority (spin-down) component around E_F. At 100 K, the splitting between the two states is ~600 meV and the occupied spin-up state is located at 160 meV below E_F.[184] The onset of the transition between bulk and surface states starts at ~1.5 eV at the $\bar{\Gamma}$ point. Optical excitation at around 1.52 eV leads to two electronic transitions: (i) from the highest occupied minority-spin bulk *d* band (Δ_2) to the minority-spin unoccupied surface state and (ii) from the majority-spin surface state to a majority-spin unoccupied bulk state. These resonant transitions induce coherent lattice vibrations perpendicular to the surface plane. As in the case of alkali-atom covered metal surfaces (Section 7), these resonances enhance the surface SHG and make TRSHG measurements extremely sensitive to oscillatory signals due to coherent vibrations.[185,186]

Bovensiepen et al.[185] have reported on coherent phonon and magnon dynamics at ferromagnetic Gd(0001) surfaces. The measurements were carried out on 20-nm-thick ferromagnetic Gd films epitaxially grown on W(110). The TRSHG measurements were performed under a magnetic field of 500 Oe along the easy axis of magnetization oriented in the film plane. A cavity damped Ti:sapphire oscillator (35 fs, 1.52 eV) was used as a light source.

The second harmonic intensity from ferromagnetic surfaces is composed of two fields, even and odd with respect to magnetization reversal.[187] The pump-induced modulations of the even and odd contributions in SHG signals reflect the dynamics of the electrons and magnetization at the surface, respectively.[188] Figure 14 shows TRSHG traces for both the even and odd components after subtraction of incoherent contributions. The Fourier transform power spectra depicted in the inset show the center frequency of 2.9 ± 0.3 THz (97 ± 10 cm^{-1}). The oscillatory part of the even component is

due to coherent vibration of the surface plane with respect to the underlying bulk, while the incoherent part is due to elevated electron temperatures from electron−electron and electron−phonon scatterings. The oscillatory signals are quenched by an yttrium overlayer deposition on the Gd surface. This observation validates the assignment of the oscillatory part to the surface coherent phonon mode.[185] The temperature dependence of the coherent amplitude follows that of the effective spin polarization at the surface.[185] These findings confirm that electronic excitations involving the exchange-split surface states are responsible for coherent phonon generation.

The electron density at the Gd(0001) surface is higher than that in the bulk, so that the surface layer relaxes inward. The optical excitation at 1.52 eV generates holes in the occupied majority band and populates electrons in the unoccupied minority band. Since the majority band is located 200 meV closer to E_F than the unoccupied minority band, the lifetime of a hole in the majority band (9 fs) is longer than that of an electron in the minority band (4 fs), as evidenced by STS line width measurements at 80 K.[184] Thus, screening of the photoinduced hole results in transient charge redistribution, which drives the surface plane out of equilibrium along the surface normal. Consequently, displacive excitation is believed to be the major cause of the observed coherent phonons.[185]

The oscillatory part observed for the odd component is due to magnon (spin wave) excitation at the surface that couples to surface phonons.[185] The exchange coupling depends on the interlayer spacing: an increase or decrease of the interlayer spacing leads to a decrease or increase of the exchange coupling, respectively, resulting in a lower or higher degree of magnetic order. Thus, the coherent surface phonon oscillation modulates the exchange coupling periodically to excite the surface magnetization parametrically.

Instead of the displacive charge-driven excitation mechanism for generation of the coherent phonons, an alternative mechanism has been recently suggested,[189] in which the pump-induced variation of the surface spin-polarization drives the coherent phonon excitation. This mechanism is based on temperature-dependent studies showing that the oscillation amplitude of even and odd contributions scales with the spin polarization of the surface state. Thus, more work is necessary to clarify this "the-chicken-or-the-egg" dilemma for the excitation mechanism.

8.2. Frequency Chirp of Coherent Phonons

In addition to coherent surface phonons, coherent bulk phonons in Gd films have also been studied by pump−probe measurements with the same configuration but probing the linear reflectivity of 800-nm probe pulses.[190] From this measurement, the Γ_3^+ coherent phonon mode was identified. Since the Γ_3^+ asymmetric mode is not expected to be excited by the DECP mechanism (see Section 3.5), it was suggested that the excitation of the bulk coherent phonon originates from coupling of surface coherent phonons to deeper layers. The center frequencies of the surface and bulk phonons averaged in the time span $t = 0-3$ ps are 2.9 THz (97 cm^{-1}) and 3.3 THz (110 cm^{-1}), respectively. Both the surface- and bulk-phonon frequencies converge at $t > 2$ ps to a value in good agreement with theoretical predictions for the Γ_3^+-mode of Gd.[191] Thus, the transient frequency of the bulk mode shows a redshift, while that of the surface mode shows a blue shift as the delay time increases.

The opposite frequency shifts of the surface and bulk phonons as a function of delay time can be explained by the electronic structure of Gd and the nonequilibrium electron distributions around the ions. The optical excitation at 1.52 eV creates nonequilibrium electron and hole distributions, which generate coherent phonons as described earlier. In the thermalization of hot electron gas, electrons are redistributed both energetically and spatially. Because the majority component of the surface state is located closer to E_F than the unoccupied minority component, an elevated electron temperature decreases the electron population in the majority spin state more strongly than it increases the minority state population. This results in a transient decrease of the electron density at the surface. Conversely, a hot electron temperature raises the electron density in the bulk. Since the electron density determines the screened ion potential, the nonequilibrium electron distributions affect the oscillation frequencies. Thus, as the electron temperature decreases, the electron density at the surface or bulk increases or decreases to the equilibrium value, respectively, resulting in blue shift or redshift of the phonon frequency.

8.3. Photon Energy Dependence

A detailed TRSHG study on the photon energy dependence of coherent surface phonon dynamics has been made in the photon energy range between 1.44 and 1.68 eV.[186] The incoherent amplitude for the even field slightly increases with photon energy up to about 1.52 eV. This is due to the pump-induced opening of a new SHG channel associated with a transition from the majority bulk band to the (normally occupied) majority surface state. At higher photon energy, the incoherent amplitude decreases because the large population of the minority surface state induced by the pump pulse reduces the density of the unoccupied intermediate states for resonant SHG. The coherent amplitudes of both phonons (even field) and magnons (odd field) show a similar photon-energy dependence of the incoherent amplitude. This confirms that the phonon excitation strength is proportional to the difference between the densities of photoinduced holes and electrons in exchange-split surface states.

Interestingly, the decay dynamics of coherent phonons and coherent magnons at the Gd surface depend on photon energy in different ways. Melnikov et al.[186] measured the decay times of the coherent part for even (phonon) and odd (magnon) fields as a function of photon energy. The coherent surface phonon decay time decreases while the coherent magnon decay time increases with an increase of the photon energy. The effect was interpreted by considering different decay mechanisms for each component. The decay of coherent surface phonons is due to electron−phonon scattering, with the scattering rate increasing with the deposited energy in the surface states. The resonant transition from the bulk minority spin state to the unoccupied surface state is enhanced as the photon energy is increased. This results in higher electron energy in the surface states, which decreases the decay time. On the other hand, this increased population of the minority surface state by irradiation with higher energy photons reduces the magnon decay rate because the magnon scattering is due to phonon-assisted spin-flip transitions whose probability is proportional to the population difference of the exchange-split surface states.

The frequencies of the coherent components also depend on photon energy. Both the phonon and magnon frequencies show a tendency toward higher frequencies beyond 1.60 eV.

As the photon energy is increased, strong pumping of electrons into the minority surface state occurs, leading to less redistribution of charge at the surface. The smaller modification of the surface ion potential gives a smaller phonon amplitude, which results in higher frequencies.

9. Control of Coherent Motion of Adsorbates

In the previous sections, we described the excitation of coherent vibrations and phonons at surfaces and how these coherent oscillations are dephased by various interactions. Since these motions are coherent in nature, we can manipulate them with sophisticated tailored laser pulses. Since the pioneering work on coherent control of phonons in organic solids by Nelson and co-workers,[192,193] various schemes have been proposed and tested: chirped pulse excitation,[194−197] feedback-controlled pulse shaping,[12,198−206] and others. Although there have been several theoretical proposals on the coherent control of surface dynamics,[207−210] experimental attempts to implement them have been scarce.

One way to realize the manipulation of coherent motions is to use phase-locked pulses. A femtosecond-pump pulse resonant with an electronic transition creates an electronic coherent polarization. Before the coherent polarization dephases completely, a pulse whose optical phase is locked to the pump pulse can interfere with the induced coherent polarization constructively or deconstructively, depending on the relative phase. This manipulation scheme is effective for isolated molecules in the gas phase,[11] since the electronic dephasing times of isolated molecules are substantially long. In contrast, since electronic dephasing occurs very rapidly at metal surfaces, applying this scheme was thought to be difficult. However, Petek and co-workers[8,13] have succeeded in demonstrating that the scheme works even for alkali-atoms strongly chemisorbed on Cu(111).

Another way to manipulate coherent motions at surfaces is to use the inherent wavelike properties of coherently excited nuclear motions, which can interfere constructively and deconstructively, depending on their initial phase relations. Here, we also describe an example of using interference phenomena to selectively excite a coherent surface phonon mode in Cs/Pt(111).[14]

9.1. Coherent Control of Nuclear Wave Packet Motions

Petek and co-workers have demonstrated that nuclear wave packet motions of adsorbates on metal surfaces can be controlled by phase-locked optical pulses.[8,13] As described in Section 7.2, a 19-fs pump laser pulse at 400 nm creates coherent polarization associated with the transition between the occupied surface state (SS) and the antibonding state (A) of Cs on Cu(111). As shown in Figure 9, since the electronic coherent polarization decay is slower than the laser pulse, the interaction of the coherent polarization with a phase-locked pulse following the pump pulse can influence the position and momentum of the nuclear wave packet.

When excitation of the SS → A transition occurs at the resonance frequency of the unexcited system, a Cs nuclear wave packet is formed on the excited-state potential energy surface. Since this surface is repulsive with respect to the Cu−Cs coordinate, the wave packet starts moving toward the vacuum. Thus, the resonance frequency decreases with increasing delay time. The nuclear wave packet dynamics

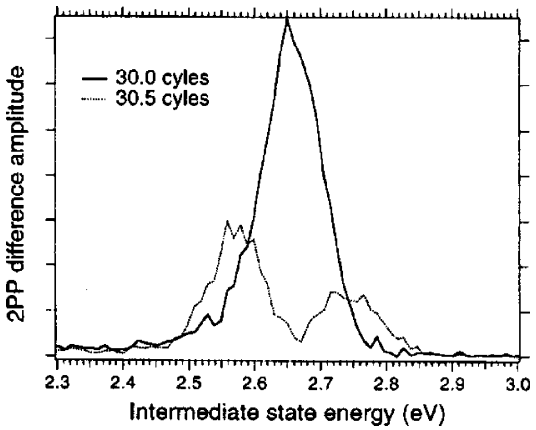

Figure 15. Two 2PPE spectra for $t = 30.0$ and 30.5 optical cycles of the resonance frequency ω_1. The spectra are depicted after subtracting the background component (taken at a long delay). In-phase excitation enhances the 2PPE signal at the SS → A resonance and suppresses it in the wings, creating a displaced wave packet on the excited-state potential energy surface, while out-of-phase excitation has the opposite effect, creating a displaced wave packet on the ground state. Reprinted with permission from ref 13. Copyright 2000 American Chemical Society.

are manifest in 2PPE spectra using phase-locked pulse pairs and chirped pulses.

First, 2PPE spectra of the SS → A resonance were taken as a function of the delay between two excitation pulses corresponding precisely to a $n2\pi$ multiple of the laser oscillation period. A series of 2PPE spectra, with the background component (the spectra at a long delay of 240 fs) subtracted, shift to lower frequency and become narrower as the delay is increased. The redshift of the peak reflects the energy of the nuclear wave packet on the excited potential energy surface with elongation of the Cu−Cs bond, while the narrowing of the spectral line is due to electronic interference between the coherent polarizations.

Next, 2PPE spectra were taken with frequency-chirped pulses. The energy and intensity of the resonance peak depend on the direction of the chirp and the rate of frequency sweep. The spectra clearly show a larger peak shift and intensity for down-chirped pulses than for up-chirped pulses. No asymmetry with regard to the direction of chirp was observed for a clean Cu(111) surface.[211] Thus, the asymmetry results from changes in the surface electronic structure caused by the Cs nuclear wave packet dynamics. Since the SS → A resonance frequency decreases as the Cu−Cs bond increases, a down-chirp is induced in the electronic polarization. Consequently, down-chirped pulses exhibit more constructive interference with the induced polarization than up-chirped pulses.

Coherent control using phase-locked pulse pair excitation is more clearly realized in 2PPE spectra taken for delays of 30.0 (40.2 fs) and 30.5 (40.2 + 0.67 fs) optical cycles of the laser frequency, as shown in Figure 15. When the optical phase of the delayed pulse is in-phase with the created coherent polarization, the peak is enhanced at the photon energy of the SS → A transition. On the other hand, for out-of-phase excitation, a dip appears at the resonance energy of the transition. This is because the phase-locked second optical pulse destructively interferes with the coherent polarization at the SS → A resonance and constructively interferes in the low- and high-energy wings. The destructive interference (stimulated reflection) at the resonance energy creates a displaced wave packet on the ground potential

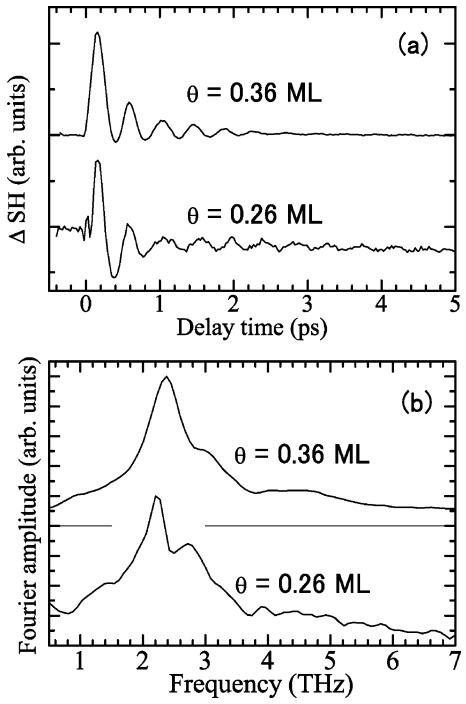

Figure 16. (a) TRSHG traces taken from Cs-covered Pt(111) and (b) Fourier transformed power spectra at Cs coverages of 0.26 and 0.36 ML. In addition to the main peak at 2.3 THz due to the Cs−Pt stretching mode, another peak appears at the higher frequency side due to a surface phonon mode.

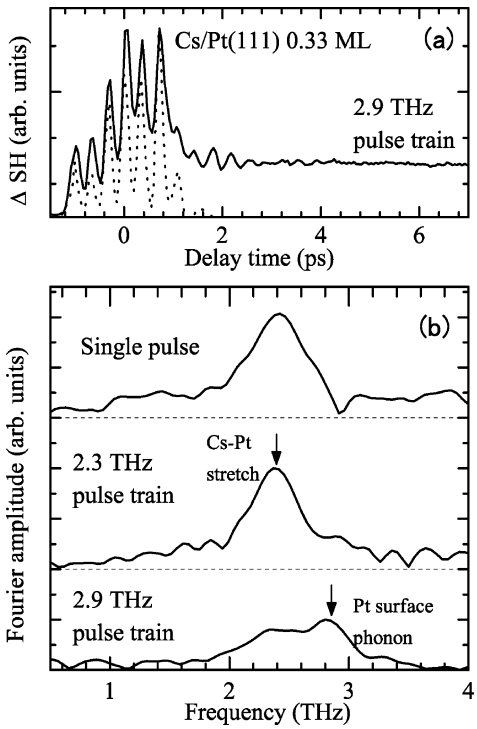

Figure 17. (a) Solid line: TRSHG trace of 0.33 ML Cs on Pt(111) for 2.9-THz repetition rate pulse-train excitation. Dashed curve: cross-correlation trace of pulse train with a nearly transform-limited pulse. (b) Fourier amplitude spectra of oscillatory components in TRSHG traces from the same surface. Top trace: single pulse excitation. Middle trace: pulse-train excitation with a repetition rate of 2.3 THz. Bottom trace: pulse train excitation with a repetition rate of 2.9 THz.

energy surface. These findings indicate that it is possible to devise optical fields to drive multiple transitions between two potential energy surfaces so as to elongate the Cs-substrate distance for desorption.

9.2. Control of Surface Phonons by Multiple Laser Pulses

9.2.1. Simultaneous Excitation of Coherent Surface Phonons on Alkali-Atom-Covered Metal Surfaces

In Section 7.3, coherent vibration of the stretching mode of alkali atoms on metal surfaces is described. The coherent vibration is generated by resonant excitation in the metallic quantum well. This electronic excitation not only generates coherent stretching vibration of alkali-atoms but also surface phonon modes.

The coverage dependence of TRSHG traces has been studied in detail for Cs/Pt(111).[9] Figure 16 shows typical TRSHG traces and their Fourier transformed spectra taken with a single pulse excitation of nearly transform-limited pulses at two different Cs coverages: $\theta = 0.26$ and 0.33 ML. In the Fourier transformed spectra, in addition to the main peak at 2.3 THz (77 cm^{-1}) of the Cs−Pt stretching mode, another peak at ∼2.8 THz (93 cm^{-1}) THz is clearly observed. Thus, the TRSHG traces cannot be fitted by a single underdamped oscillating component. Based on a fit by LPSVD,[57,212] the oscillatory part in $t > 250$ fs is well expressed by a linear combination of underdamped oscillators, $\sum_i A_i \exp(-t/\tau_i) \cos(\omega_i t + \phi_i)$. For both coverages, the oscillatory part in $t > 250$ fs can be decomposed into two components: the Cs−Pt stretching mode and the Pt surface phonons modes (Rayleigh modes) with frequencies of 2.3 and 2.7 THz (77 and 90 cm^{-1}) at $\theta = 0.26$ ML, respectively, and slightly shifted to 2.4 and 2.9 THz (80 and 97 cm^{-1}) at $\theta = 0.33$ ML. Cs adsorbates form the (2×2) superstructure at $\theta = 0.26$ ML and the $(\sqrt{3} \times \sqrt{3})R30°$ superstructure at $\theta = 0.33$ ML, as in the case of K/Pt(111)[213] described in Section 7.1. Because of the adsorbate superstructures at the corresponding coverage, the Rayleigh modes at the surface Brillouin zone boundaries of a clean platinum surface are folded onto the $\bar{\Gamma}$ point and become optically active.

9.2.2. Selective Excitation by Tailored Pulses

Watanabe et al.[14] have demonstrated that a coherent mode can be selectively excited by using tailored femtosecond-pulse trains. The pulse trains are synthesized by a pulse shaper consisting of a liquid-crystal spatial light modulator, a pair of gratings, and cylindrical lenses in a 4*f* configuration.[214] A periodic pattern of phase retardation with a period δF was implemented in the liquid crystal array of the modulator that generates the pulse train with a period of $1/\delta F$. Binary phase-only filters, called Dammann gratings,[215,216] for the pulse-train generation produce flat-topped pulse trains with temporal cutoff edges. The filter pattern of the Dammann gratings for the number of pulses in a pulse train $N = 5$ or 7 were used based on the prescription given in ref 216.

TRSHG traces were taken for 0.33 ML Cs covered Pt(111) excited by a pulse-train with $N = 7$ and a repetition rate tuned from 2.0 to 2.9 THz. Figure 17a shows a TRSHG trace obtained by a pulse-train with repetition rate 2.9 THz as an example. The dashed line is a cross-correlation trace of the pulse-train with a nearly transform-limited pulse. According to a theoretical analysis of multiple pulse excitation by Yan and Mukamel,[217] the electric field of an ultrashort pulse train acts as a frequency-domain filter with the power spectrum of the pump field. This is clearly shown in Figure 17b. For a pulse train with a 2.3-THz repetition rate, the

Fourier spectrum of the TRSHG trace shows a strong peak at the same frequency as that of the pulse train envelope. However, as the repetition rate is increased to 2.9 THz, the peak intensity at 2.3 THz decreases while that of the higher frequency component of the Rayleigh phonon mode increases.

The amplitude ratios between the Rayleigh mode and the Cs−Pt stretching mode obtained by single pulse excitation are 0.72 and 0.25 at $\theta = 0.26$ and 0.33 ML, respectively. These ratios increase to 3.16 and 0.89 when a 2.9-THz pulse train is used. Thus, at both coverages the ratios are increased by a factor of ~4. Consequently, these observations indicate that one can selectively excite either the Cs−Pt stretching mode or the Rayleigh phonon mode by tuning the repetition rate of the pulse train.

10. Summary and Outlook

The advent of femtosecond-laser pulse technology allows us to investigate coherent nuclear oscillations at surfaces and interfaces. Time-resolved nonlinear spectroscopy techniques such as TRSHG and TRSFG described in this review are very powerful for monitoring how coherent oscillations are created and dephased after a pump pulse. These spectroscopy techniques are all surface sensitive and play a complementary role in studies on the dynamics of adsorbate vibrations and surface phonons. While TRSFG, in particular, with broad femtosecond-IR and narrow band visible pulses is very useful for monitoring IR- and Raman-active vibrational modes of adsorbates in the relatively high-frequency range, TRSHG is suitable for monitoring coherent vibrations and phonons at surfaces in the low-frequency range.

Vibrational relaxation of CO on metal surfaces has been further studied by femtosecond TRSFG. In addition to extensive works on line profile analysis and picosecond time-resolved spectroscopy, the works on femtosecond TRSFG described in this review have firmly established a foundation for vibrational relaxation of the internal CO stretching mode at metal surfaces. This mode can be excited to higher vibrational states than the $v = 1$ state by intense IR pulses. This allows us to tackle the interesting issue of how a localized vibrational mode at a surface is delocalized by inter-adsorbate interactions.

For a further understanding of vibrational relaxation of adsorbates, studies on adsorption systems other than CO are needed. Moreover, the newly developed 2-D vibrational spectroscopy technique should provide a new dimension for studies of inter-adsorbate interactions.

TRSHG was first applied to semiconductor surfaces and interfaces, and its applications have been extended to alkali-atom covered metal surfaces and ferromagnetic Gd thin films. These studies have shown that TRSHG is a very versatile technique for monitoring relatively low-frequency phonons at surfaces. Coherent phonon modes provide an interesting opportunity for exploring coupling between electrons and nuclei at surfaces, since adsorbate-induced or surface-localized electronic states near the Fermi level are involved in both the excitation and dephasing of coherent oscillations. Theoretical works are needed for a further understanding of the excitation and dephasing dynamics of low-frequency coherent surface phonon modes.

The coherent control of nuclear dynamics at surfaces is still in its early stages. Rapid electronic dephasing at metal surfaces is a serious obstacle for the realization of coherent control, and there is still little information on the dephasing of electrons and phonons at surfaces. Thus, the dephasing dynamics should be further studied on metal and semiconductor surfaces using the available tools such as TRSHG, TRSFG, and ITR-2PPE.

11. Acknowledgments

This work was supported in part by Grants-in-Aid for Scientific Research (S) (17105001) from the Japan Society for the Promotion of Science (JSPS), Scientific Research on Priority Area (417 Fundamental Science and Technology of Photofunctional Interfaces, and 432 Molecular Nano Dynamics), and Creative Scientific Research Collaboratory on Electron Correlation-Toward a New Research Network between Physics and Chemistry (13NP0201) from the Ministry of Education, Culture, Sports, Science and Technology (MEXT) of Japan.

12. References

(1) Somorjai, G. A. *Introduction to Surface Chemistry and Catalysis*; Wiley: New York, 1994.
(2) Masel, R. I. *Principles of Adsorption and Reaction on Solid Surfaces*; John Wiley & Sons: New York, 1996.
(3) Chabal, Y. J. *Surf. Sci. Rep.* **1988**, *8*, 211.
(4) Heilweil, E. J.; Casassa, M. P.; Cavanagh, R. R.; Stephenson, J. C. *Annu. Rev. Phys. Chem.* **1989**, *40*, 143.
(5) Cavanagh, R. R.; Heilweil, E. J.; Stephenson, J. C. *Surf. Sci.* **1994**, *299/300*, 643.
(6) Beckerle, J. D. Spectroscopy and Dynamics of Vibrationally Excited Adsorbates on Metal Surfaces. In *Laser Spectroscopy and Photochemistry on Metal Surfaces*, Dai, H.-L., Ho, W., Eds.; World Scientific: Singapore, 1995; Chapter 12, pp 459−497.
(7) Ueba, H. *Prog. Surf. Sci.* **1997**, *55*, 115.
(8) Petek, H.; Ogawa, S. *Annu. Rev. Phys. Chem.* **2002**, *53*, 507.
(9) Watanabe, K.; Takagai, N.; Matsumoto, Y. *Phys. Rev. B* **2005**, *71*, 085414.
(10) Polanyi, J. C.; Zewail, A. H. *Acc. Chem. Res.* **1995**, *28*, 119.
(11) Rice, S. A.; Zhao, M. *Optical Control of Molecular Dynamics*; John Wiley: New York, 2000.
(12) Assion, A.; Baumert, T.; Bergt, M.; Brixner, T.; Kiefer, B.; Seyfried, V.; Strehle, M.; Gerber, G. *Science* **1998**, *282*, 919.
(13) Petek, H.; Nagano, H.; Weida, M. J.; Ogawa, S. *J. Phys. Chem. B* **2000**, *104*, 10234.
(14) Watanabe, K.; Takagai, N.; Matsumoto, Y. *Phys. Chem. Chem. Phys.* **2005**, *7*, 2697.
(15) Bargheer, M.; Zhavoronkov, N.; Gritsai, Y.; Woo, J. C.; Kim, D. S.; Woerner, M.; Elsaesser, T. *Science* **2004**, *306*, 1771.
(16) Sokolowski-Tinten, K.; Blome, C.; Blums, J.; Cavalleri, A.; Dietrich, C.; Tarasevitch, A.; Uschmann, I.; Förster, E.; Kammler, M.; Hoegen, M. H. V.; der Linde, D. V. *Nature* **2003**, *422*, 287.
(17) Blum, K. *Density Matrix Theory and Applications*; Plenum Press: New York, 1981.
(18) Cohen-Tannoudji, C.; Diu, B.; Laloë, F. *Quantum Mechanics*; Hermann and John Wiley: New York, 1977.
(19) Boyd, R. W. *Nonlinear Optics*; Academic Press: San Diego, 2003.
(20) Hellsing, B.; Persson, M. *Phys. Scr.* **1984**, *29*, 360.
(21) Gadzuk, J. W.; Luntz, A. C. *Surf. Sci.* **1984**, *144*, 429.
(22) Persson, B. N. J.; Hoffmann, F. M.; Ryberg, R. *Phys. Rev. B* **1986**, *34*, 2266.
(23) Laubereau, A.; Kaiser, W. *Rev. Mod. Phys.* **1978**, *50*, 607.
(24) Heilweil, E. J.; Casassa, M. P.; Cavanagh, R. R.; Stephenson, J. C. *J. Chem. Phys.* **1984**, *81*, 2856.
(25) Guyot-Sionnest, P.; Dumas, P.; Chabal, Y. J. *J. Electron Spectrosc. Relat. Phenom.* **1990**, *54−55*, 27.
(26) Guyot-Sionnest, P.; Dumas, P.; Chabal, Y. J.; Higashi, G. S. *Phys. Rev. Lett.* **1990**, *64*, 2156.
(27) Guyot-Sionnest, P.; Harris, A. L. Surface Vibrational Dynamics Probed by Sum Frequency Generation. In *Laser Spectroscopy and Photochemistry on Metal Surfaces*, Dai, H.-L., Ho, W., Eds.; World Scientific: Singapore, 1995; Chapter 11, pp 405−458.
(28) Zeiger, H. J.; Vidal, J.; Cheng, T. K.; Ippen, E. P.; Dresselhaus, G.; Dresselhaus, M. S. *Phys. Rev. B* **1992**, *45*, 768.
(29) Scholz, R.; Pfeifer, T.; Kurz, H. *Phys. Rev. B* **1993**, *47*, 16229.
(30) Kuznetsov, A. V.; Stanton, C. J. *Phys. Rev. Lett.* **1994**, *73*, 3243.
(31) Garrett, G. A.; Albrecht, T.; Whitaker, J. F.; Merlin, R. *Phys. Rev. Lett.* **1996**, *77*, 3661.
(32) Merlin, R. *Solid State Commun.* **1997**, *102*, 207.

(33) Lobad, A. I.; Taylor, A. J. *Phys. Rev. B* **2001**, *64*, 180301.
(34) Stevens, T. E.; Kuhl, J.; Merlin, R. *Phys. Rev., B* **2002**, *65*, 144304.
(35) Dekorsy, T.; Cho, G. C.; Kurz, H. Coherent Phonons in Condensed Media. In *Light Scattering in Solids VIII*, Vol. 76; Cardona, M.; Güntherodt, G., Ed.; Springer-Verlag: Berlin Heidelberg, 2000; Chapter 4, pages 169−209.
(36) Chang, Y.-M.; Xu, L.; Tom, H. K. *Chem. Phys.* **2000**, *251*, 283.
(37) Shen, Y. R. *The Principles of Nonlinear Optics*; John Wiley: New Jersey, 2003.
(38) Mukamel, S. *Principles of Nonlinear Optical Spectroscopy*; Oxford University Press: New York, 1995.
(39) Dhar, L.; Rogers, J. A.; Nelson, K. A. *Chem. Rev.* **1994**, *94*, 157.
(40) Chesnoy, J.; Mokhtari, A. *Phys. Rev. A* **1988**, *38*, 3566.
(41) Cho, G. C.; Kutt, W.; Kurz, H. *Phys. Rev. Lett.* **1990**, *65*, 764.
(42) Misochko, O. V.; Hase, M.; Kitajima, M. *Phys. Solid State* **2004**, *46*, 1741.
(43) Hunsche, S.; Wienecke, K.; Dekorsy, T.; Kurz, H. *Phys. Rev. Lett.* **1995**, *75*, 1815.
(44) Zhu, X. D.; Suhr, H.; Shen, Y. R. *Phys. Rev. B* **1987**, *35*, 3047.
(45) Hunt, J. H.; Guyot-Sionnest, P.; Shen, Y. R. *Chem. Phys. Lett.* **1987**, *133*, 189.
(46) Shen, Y. R. *Nature* **1989**, *337*, 519.
(47) Harris, A. L.; Chidsey, C. E. D.; Levinos, N. J.; Loiacono, D. N. *Chem. Phys. Lett.* **1987**, *141*, 350.
(48) Guyot-Sionnest, P.; Tadjeddine, A. *Chem. Phys. Lett.* **1990**, *172*, 341.
(49) Guyot-Sionnest, P. *Surf. Sci.* **2005**, *585*, 1.
(50) Richter, L. J.; Petralli-Mallow, T. P.; Stephenson, J. C. *Opt. Lett.* **1998**, *23*, 1594.
(51) Roke, S.; Kleyn, A.; Bonn, M. *J. Phys. Chem. A* **2001**, *105*, 1683.
(52) Ishibashi, T.-A.; Onishi, H. *Chem. Phys. Lett.* **2001**, *346*, 413.
(53) Ch. Hess, M. Wolf, S. R.; Bonn, M. *Surf. Sci.* **2002**, *502/503*, 304.
(54) Ueba, H.; Sawabu, T.; Mii, T. *Surf. Sci.* **2002**, *502/503*, 254.
(55) Chang, Y.-M.; Xu, L.; Tom, H. W. K. *Phys. Rev. Lett.* **1997**, *78*, 4649.
(56) Fujiyoshi, S.; Ishibashi, T.; Onishi, H. *J. Phys. Chem. B* **2004**, *108*, 10636.
(57) Barkhuijsen, H.; de Beer, R.; Boveé, W. M. M. J.; Ormondt, D. V. *J. Magn. Reson.* **1985**, *61*, 465.
(58) Johnson, A. E.; Myers, A. B. *J. Chem. Phys.* **1996**, *104*, 2497.
(59) Ueba, H. *Prog. Surf. Sci.* **1986**, *22*, 181.
(60) Blyholder, G. *J. Phys. Chem.* **1964**, *68*, 2722.
(61) Föhlisch, A.; Nyberg, M.; Hasselström, J.; Karis, O.; Pettersson, L. M.; Nilsson, A. *Phys. Rev. Lett.* **2000**, *85*, 3309.
(62) Föhlisch, N.; Nyberg, M.; Bennich, P.; Triguero, L.; Hasselström, J.; Karis, O.; Pettersson, L. G. M.; Nilsson, A. *J. Chem. Phys.* **2000**, 1946.
(63) Dose, V.; Bradshaw, J. R. M.; Prince, K. C. *Surf. Sci.* **1987**, *179*, 90.
(64) Anazawa, T.; Kinoshita, I.; Matsumoto, Y. *J. Electron Spectrosc. Relat. Phenom.* **1998**, *88*−*91*, 585.
(65) Chou, K. C.; Westerberg, S.; Shen, Y. R.; Ross, P. N.; Somorjai, G. A. *Phys. Rev.* **2004**, *69*, 153413.
(66) Klünker, C.; Balden, M.; Lehwald, S.; Daum, W. *Surf. Sci.* **1996**, *360*, 104.
(67) Persson, B. N. J.; Persson, M. *Solid State Commun.* **1980**, *36*, 175.
(68) Crljen, Z.; Langreth, D. *Phys. Rev. B* **1987**, *35*, 4224.
(69) Ryberg, R. *Phys. Rev. B* **1985**, *32*, 2671.
(70) Morin, M.; Levinos, N. J.; Harris, A. L. *J. Chem. Phys.* **1992**, *96*, 3950.
(71) Rantala, T. T.; Rosén, A. *Phys. Rev. B* **1986**, *34*, 837.
(72) Head-Gordon, M.; Tully, J. C. *J. Chem. Phys.* **1992**, *96*, 3939.
(73) Trenary, M.; Uram, K. J.; Bozso, F.; Yates, J. T., Jr. *Surf. Sci.* **1984**, *146*, 269.
(74) Persson, B. N. J.; Ryberg, R. *Phys. Rev. B* **1985**, *32*, 3586.
(75) Schweizer, E.; Persson, B. N. J.; Tüshaus, M.; Hoge, D.; Bradshaw, A. M. *Surf. Sci.* **1989**, *213*, 49.
(76) Persson, B. N. J.; Zaremba, E. *Phys. Rev. B* **1985**, *31*, 1863.
(77) Persson, B. N. J.; Gadzuk, J. W. *Surf. Sci. Lett.* **1998**, *410*, L779.
(78) Germer, T. A.; Stephenson, J. C.; Heilweil, E. J.; Cavanagh, R. R. *J. Chem. Phys.* **1994**, *101*, 1704.
(79) Shelby, R. M.; Harris, C. B.; Cornelius, P. A. *J. Chem. Phys.* **1979**, *70*, 34.
(80) Persson, B. N. J.; Ryberg, R. *Phys. Rev. B* **1989**, *40*, 10273.
(81) Germer, T. A.; Stephenson, J. C.; Heilweil, E. J.; Cavanagh, R. R. *J. Chem. Phys.* **1993**, *98*, 9986.
(82) Graham, A.; Hofmann, F.; Toennies, J. P. *J. Chem. Phys.* **1996**, *104*, 5311.
(83) Crim, F. F. *J. Phys. Chem.* **1996**, *100*, 12725.
(84) Zare, R. N. *Science* **1998**, *279*, 1875.
(85) Crim, F. F. *Acc. Chem. Res.* **1999**, *32*, 877.
(86) Herzberg, G. *Molecular Spectra and Molecular Structure II*; Van Nostrand Reinhold: New York, 1945.
(87) Bondybey, V. E. *Annu. Rev. Phys. Chem.* **1984**, *35*, 591.
(88) Nesbitt, D. J.; Field, R. W. *J. Phys. Chem.* **1996**, *100*, 12735.
(89) Kimball, J. C.; Fong, C. Y.; Shen, Y. R. *Phys. Rev. B* **1981**, *23*, 4946.
(90) Chabal, Y. J. *Phys. Rev. Lett.* **1985**, *55*, 845.
(91) Persson, B. N. J.; Ryberg, R. *Chem. Phys. Lett.* **1990**, *174*, 443.
(92) Ryberg, R. *Phys. Rev. B* **1991**, *44*, 13160.
(93) Guyot-Sionnest, P. *Phys. Rev. Lett.* **1991**, *67*, 2323.
(94) Jakob, P. *Phys. Rev. Lett.* **1996**, *77*, 4229.
(95) Jakob, P.; Persson, B. N. J. *J. Chem. Phys.* **1998**, *109*, 8641.
(96) Jakob, P. *Surf. Sci.* **1999**, *427/428*, 309.
(97) Hess, C.; Bonn, M.; Funk, S.; Wolf, M. *Chem. Phys. Lett.* **2000**, *325*, 139.
(98) Bonn, M.; Hess, C.; Roeterdink, W. G.; Ueba, H.; Wolf, M. *Chem. Phys. Lett.* **2004**, *388*, 269.
(99) Hess, C.; Wolf, M.; Bonn, M. *Phys. Rev. Lett.* **2000**, *85*, 4341.
(100) Harris, C. B.; Shelby, R. M.; Corneilius, P. A. *Phys. Rev. Lett.* **1977**, *38*, 1415.
(101) Bonn, M.; Hess, C.; Wolf, M. *J. Chem. Phys.* **2001**, *115*, 7725.
(102) Förster, T. *Discuss. Faraday Soc.* **1959**, *27*, 7.
(103) Zhang, V. L.; Arnolds, H.; King, D. A. *Surf. Sci.* **2005**, *587*, 102.
(104) Beckerle, J. D.; Cavanagh, R. R.; Casassa, M. P.; Heilweil, E. J.; Stephenson, J. C. *J. Chem. Phys.* **1991**, *95*, 5403.
(105) Park, K.; Cho, M. *J. Chem. Phys.* **1998**, *109*, 10559.
(106) Cho, M. *Phys. Rev. A* **2000**, *61*, 023406.
(107) Zhao, W.; Wright, J. C. *Phys. Rev. Lett.* **2000**, *84*, 1411.
(108) Hamm, P.; Lim, M.; DeGrado, W. F.; Hochstrasser, R. M. *J. Chem. Phys.* **2000**, *112*, 1907.
(109) Bonn, M.; Hess, C.; Miners, J. H.; Heinz, T. F.; Bakker, H. J.; Cho, M. *Phys. Rev. Lett.* **2001**, *86*, 1566.
(110) Cho, G. C.; Kutt, W.; Kurz, H. *Phys. Rev. B* **1990**, *65*, 764.
(111) Cheng, T. K.; Brorson, S. D.; Kazeroonian, A. S.; Moodera, J. S.; Dresselhaus, G.; Dresselhaus, M. S.; Ippen, E. P. *Appl. Phys. Lett.* **1990**, *57*, 1004.
(112) Cheng, T. K.; Acioli, L. H.; Vidal, J.; Zeiger, H. J.; Dresselhaus, G.; Dresselhaus, M. S.; Ippen, E. P. *Appl. Phys. Lett.* **1993**, *62*, 1901.
(113) Mazin, I. I.; Liechtenstein, A. I.; Jepsen, O.; Andersen, O. K.; Rodriguez, C. O. *Phys. Rev. B* **1994**, *49*, 9210.
(114) Hase, M.; Mizoguchi, K.; Harima, H.; Nakashima, S.; Tani, M.; Sakai, K.; Hangyo, M. *Appl. Phys. Lett.* **1996**, *69*, 2474.
(115) Hase, M.; Mizoguchi, K.; Harima, H.; Nakashima, S. I.; Sakai, K. *Phys. Rev. B* **1998**, *58*, 5448.
(116) Bakker, H. J.; Hunsche, S.; Kurz, H. *Rev. Mod. Phys.* **1998**, *70*, 523.
(117) Tangney, P.; Fahy, S. *Phys. Rev. Lett.* **1999**, *82*, 4340.
(118) Mishina, T.; Nitta, K.; Masumoto, Y. *Phys. Rev. B* **2000**, *62*, 2908.
(119) Hase, M.; Ishioka, K.; Kitajima, M.; Ushida, K.; Hishita, S. *Appl. Phys. Lett.* **2000**, *76*, 1258.
(120) Hase, M.; Kitajima, M.; Nakashima, S.; Mizoguchi, K. *Phys. Rev. Lett.* **2002**, *88*, 067401.
(121) Yee, K. J.; Lee, K. G.; Oh, E.; Kim, D. S.; Lim, Y. S. *Phys. Rev. Lett.* **2002**, *88*, 105501.
(122) Kim, A. M. T.; Roeser, C. A. D.; Mazur, E. *Phys. Rev. B* **2003**, *68*, 012301.
(123) Misochko, O. V.; Hase, M.; Ishioka, K.; Kitajima, M. *Phys. Rev. Lett.* **2004**, *92*, 197401.
(124) Fahy, S.; Reis, D. A. *Phys. Rev. Lett.* **2004**, *93*, 109701.
(125) Murray, E. D.; Fritz, D. M.; Wahlstrand, J. K.; Fahy, S.; Reis, D. A. *Phys. Rev. B* **2005**, *72*, 060301.
(126) Chang, Y.-M.; Xu, L.; Tom, H. W. K. *Phys. Rev. B* **1999**, *59*, 12220.
(127) Watanabe, K.; Dimitrov, D. T.; Takagi, N.; Matsumoto, Y. *Phys. Rev. B* **2002**, *65*, 235328.
(128) Bron, W. E.; Mehta, S.; Kuhl, J.; Klingenstein, M. *Phys. Rev. B* **1989**, *39*, 12642.
(129) Chang, Y.-M.; Chuang, C. T.; Chia, C. T.; Tsen, K. T.; Lu, H.; Schaff, W. J. *Appl. Phys. Lett.* **2004**, *85*, 5224.
(130) Chang, Y.-M. *Appl. Phys. Lett.* **2003**, *82*, 1781.
(131) Chang, Y.-M.; Lin, H. H.; Chia, C. T.; Chen, Y. F. *Appl. Phys. Lett.* **2004**, *84*, 2548.
(132) Haight, R. *Surf. Sci. Rep.* **1995**, *21*, 275.
(133) Weinelt, M.; Kutschera, M.; Fauster, T.; Rohlfing, M. *Phys. Rev. Lett.* **2004**, *92*, 126801.
(134) Voelkmann, C.; Reichelt, M.; Meier, T.; Koch, S.; Höfer, U. *Phys. Rev. Lett.* **2004**, *92*, 127405.
(135) Hase, M.; Kitajima, M.; Constantinescu, A. M.; Petek, H. *Nature* **2003**, *426*, 51.
(136) Heys, J. V.; Lindenblatt, M.; Pehlke, E. *Phase Transitions* **2005**, *78*, 773.
(137) Bonse, J. *Appl. Phys. A* **2006**, *84*, 63.
(138) Mross, W. D. *Catal. Rev.-Sci. Eng.* **1983**, *25*, 591.
(139) Bonzel, H. P. *Surf. Sci. Rep.* **1988**, *8*, 43.
(140) Bonzel, H. P. *Physics and Chemistry of Alkali Metal Adsorption;* Elsevier: Amsterdam, 1989.
(141) Dushman, S. *Rev. Mod. Phys.* **1930**, *2*, 381.

(142) Dushman, S., Lafferty, J. M., Eds.; *Scientific Foundations of Vacuum Technique*; John Wiley & Sons: New York, 1962.
(143) Kaminsky, M. *Atomic and Ioninc Impact Phenomena on Metal Surfaces*; Academic Press: New York, 1965.
(144) Ogawa, S.; Nagano, H.; Petek, H. *Phys. Rev. Lett.* **1999**, *82*, 1931.
(145) Petek, H.; Weida, M. J.; Nagano, H.; Ogawa, S. *Science* **2000**, *288*, 1402.
(146) Petek, H.; Weida, M.; Nagano, H.; Ogawa, S. *Surf. Sci.* **2000**, *451*, 22.
(147) Watanabe, K.; Takagi, N.; Matsumoto, Y. *Chem. Phys. Lett.* **2002**, *366*, 606.
(148) Watanabe, K.; Takagi, N.; Matsumoto, Y. *Phys. Rev. Lett.* **2004**, *92*, 57401.
(149) Matsumoto, Y.; Watanabe, K.; Takagi, N. *Surf. Sci.* **2005**, *593*, 110.
(150) Aruga, T.; Murata, Y. *Prog. Surf. Sci.* **1989**, *31*, 61.
(151) Campbell, C. T. *Annu. Rev. Phys. Chem.* **1990**, *41*, 775.
(152) Naumovets, A. G. *Surf. Sci.* **1994**, *299/300*, 706.
(153) Diehl, R. D.; McGrath, R. *Surf. Sci. Rep.* **1996**, *23*, 43.
(154) Tochihara, H.; Mizuno, S. *Surf. Sci.* **1992**, *279*, 89.
(155) Mizuno, S.; Tochihara, H.; Barbieri, A.; Hove, M. A. V. *Phys. Rev. B* **1995**, *51*, 1969.
(156) Mizuno, S.; Tochihara, H.; Matsumoto, Y.; Tanaka, K.-I. *Surf. Sci. Lett.* **1997**, *393*, L69.
(157) Pirug, G.; Bonzel, H. P. *Surf. Sci.* **1988**, *194*, 159.
(158) Gurney, R. W. *Phys. Rev.* **1935**, *47*, 479.
(159) Ishida, H. *Phys. Rev. B* **1990**, *42*, 10899.
(160) Fischer, N.; Schuppler, S.; Fischer, R.; Fauster, T.; Steinmann, W. *Phys. Rev. B* **1991**, *43*, 14722.
(161) Fischer, N.; Schuppler, S.; Fauster, T.; Steinmann, W. *Surf. Sci.* **1994**, *314*, 89.
(162) Tang, D.; McIlroy, D.; Shi, X.; Heskett, D. *Surf. Sci. Lett.* **1991**, *255*, L497.
(163) Petek, H.; Ogawa, S. *Prog. Surf. Sci.* **1997**, *56*, 239.
(164) Bauer, M.; Pawlik, S.; Aeschlimann, M. *Phys. Rev. B* **1997**, *55*, 10040.
(165) Bauer, M.; Pawlik, S.; Aeschlimann, M. *Phys. Rev. B* **1999**, *60*, 5016.
(166) Borisov, A. G.; Kazansky, A. K.; Gauyacq, J. P. *Surf. Sci.* **1999**, *430*, 165.
(167) Borisov, A. G.; Gauyacq, J. P.; Kazansky, A. K.; Chulkov, E. V.; Silkin, V. M.; Echenique, P. M. *Phys. Rev. Lett.* **2001**, *86*, 488.
(168) Ishida, H.; Liebsch, A. *Phys. Rev. B* **1992**, *45*, 6171.
(169) Hellsing, B.; Chakarov, D. V.; Österlund, L.; Zhdanov, V. P.; Kasemo, B. *J. Chem. Phys.* **1997**, *106*, 982.
(170) Dudde, R.; Johansson, L. S. Q.; Reihl, B. *Phys. Rev. Lett.* **1991**, *44*, 1198.
(171) Hoffmann, G.; Kliewer, J.; Berndt, R. *Phys. Rev. Lett.* **2001**, *87*, 176803.
(172) Chulkov, E. V.; Kliewer, J.; Berndt, R.; Silkin, V. M.; Hellsing, B.; Crampin, S.; Echenique, P. M. *Phys. Rev. B* **2003**, *68*, 195422.
(173) Hoffmann, G.; Berndt, R.; Johansson, P. *Phys. Rev. Lett.* **2003**, *90*, 46803.
(174) Kliewer, J.; Berndt, R. *Phys. Rev. B* **2002**, *65*, 035412.
(175) Carlsson, A.; Hellsing, B.; Lindgren, S.-Å.; Walldén, L. *Phys. Rev. B* **1997**, *56*, 1593.
(176) Carlsson, J. M.; Hellsing, B. *Phys. Rev. B* **2000**, *61*, 13973.
(177) Witte, G.; Toennies, J. P. *Phys. Rev. B* **2000**, *62*, R7771.
(178) He, P.; Jacobi, K. *Phys. Rev. B* **1996**, *53*, 3658.
(179) Klünker, C.; Steimer, C.; Hannon, J. B.; Giesen, M.; Ibach, H. *Surf. Sci.* **1999**, *420*, 25.
(180) Song, K. J.; Heskett, D.; Dai, H. L.; Liebsch, A.; Plummer, E. W. *Phys. Rev. Lett.* **1988**, *61*, 1380.
(181) Lindgren, S. A.; Wallden, L. *Phys. Rev. B* **1992**, *45*, 6345.
(182) Persson, M.; Hellsing, B. *Phys. Rev. Lett.* **1982**, *49*, 662.
(183) Persson, B. N. J.; Tosatti, E.; Fuhrmann, D.; Witte, G.; Wöll, C. *Phys. Rev. B* **1999**, *59*, 11777.
(184) Rehbein, A.; Wegner, D.; Kaindl, G.; Bauer, A. *Phys. Rev. B* **2003**, *67*, 033403.
(185) Melnikov, A.; Radu, I.; Bovensiepen, U.; Krupin, O.; Starke, K.; Matthias, E.; Wolf, M. *Phys. Rev. Lett.* **2003**, *91*, 227403.
(186) Melnikov, A. V.; Radu, I.; Bovensiepen, U.; Starke, K.; Wolf, M.; Matthias, E. *J. Opt. Soc. Am. B* **2005**, *22*, 204.
(187) Pan, R. P.; Wei, H. D.; Shen, Y. R. *Phys. Rev. B* **1989**, *39*, 1229.
(188) Hohlfeld, J.; Matthias, E.; Knorren, R.; Bennemann, K. H. *Phys. Rev. Lett.* **1997**, *78*, 4861.
(189) Bovensiepen, U. *Appl. Phys. A* **2006**, *82*, 395.
(190) Bovensiepen, U.; Melnikov, A.; Radu, I.; Krupin, O.; Starke, K.; Wolf, M.; Matthias, E. *Phys. Rev. B* **2004**, *69*, 235417.
(191) Rao, R. R.; Menon, C. S. *J. Phys. Chem. Solids* **1974**, *35*, 425.
(192) Weiner, A. M.; Leaird, D. E.; Wiederrecht, G. P.; Nelson, K. A. *Science* **1990**, *247*, 1317.
(193) Weiner, A. M.; Leaird, D. E.; Wiederrecht, G. P.; Nelson, K. A. *J. Opt. Soc. Am. B* **1991**, *8*, 1264.
(194) Bardeen, C. J.; Wang, Q.; Shank, C. V. *Phys. Rev. Lett.* **1995**, *75*, 3410.
(195) Cerullo, G.; Bardeen, C. J.; Wang, Q.; Shank, C. V. *Chem. Phys. Lett.* **1996**, *262*, 362.
(196) Bardeen, C. J.; Che, J.; Wilson, K. R.; Yakovlev, V. V.; Apkarian, V. A.; Martens, C. C.; Zadoyan, R.; Kohler, B.; Messina, M. *J. Chem. Phys.* **1997**, *106*, 8486.
(197) Misawa, K.; Kobayashi, T. *J. Chem. Phys.* **2000**, *113*, 7546.
(198) Bardeen, C. J.; Yakovlev, V. V.; Wilson, K. R.; Carpenter, S. D.; Weber, P. M.; Warren, W. S. *Chem. Phys. Lett.* **1997**, *280*, 151.
(199) Hornung, T.; Meier, R.; Motzkus, M. *Chem. Phys. Lett.* **2000**, *326*, 445.
(200) Grass, A.; Rozgonyi, T.; Feurer, T.; Sauerbrey, R.; Szabo, G. *Appl. Phys. B* **2000**, *71*, 267.
(201) Weinacht, T. C.; White, J. L.; Bucksbaum, P. H. *J. Phys. Chem. A* **1999**, *103*, 10166.
(202) Brixner, T.; Damrauer, N. H.; Niklaus, P.; Gerber, G. *Nature* **2001**, *414*, 57.
(203) Levis, R. J.; Menkir, G. M.; Rabitz, H. *Science* **2001**, *292*, 709.
(204) Herek, J. L.; Wohlleben, W.; Cogdell, R. J.; Zeidler, D.; Motzkus, M. *Nature* **2002**, *417*, 533.
(205) Zeidler, D.; Frey, S.; Wohlleben, W.; Motzkus, M.; Busch, F.; Chen, T.; Kiefer, W.; Materny, A. *J. Chem. Phys.* **2002**, *116*, 5231.
(206) Daniel, C.; Full, J.; González, L.; Lupulescu, C.; Manz, J.; Merli, A.; Vajda, Š.; Wöste, L. *Science* **2003**, *299*, 536.
(207) Deyirmenjian, V. B.; Sipe, J. E. *Phys. Rev. Lett.* **1999**, *82*, 4942.
(208) Santana, A.; Micha, D. A. *Chem. Phys. Lett.* **2003**, *369*, 459.
(209) Mishima, K.; Yamashita, K. *J. Chem. Phys.* **1999**, *110*, 7756.
(210) Nakagami, K.; Ohtsuki, Y.; Fijimura, Y. *Chem. Phys. Lett.* **2002**, *360*, 91.
(211) Petek, H.; Heberle, A. P.; Nessler, W.; Nagano, H.; Kubota, S.; Matsunami, S.; Moriya, N.; Ogawa, S. *Phys. Rev. Lett.* **1997**, *79*, 4649.
(212) Johnson, A. E.; Myers, A. B. *J. Chem. Phys.* **1996**, *104*, 2497.
(213) Cousty, J.; Riwan, R. *Surf. Sci.* **1988**, *204*, 45.
(214) Wefers, M. M.; Nelson, K. A. *J. Opt. Soc. Am. B* **1995**, *12*, 1343.
(215) Weiner, A. M.; Leaird, D. E. *Opt. Lett.* **1990**, *15*, 51.
(216) Killat, U.; Rabe, G.; Rave, W. *Fiber Integr. Opt.* **1982**, *4*, 159.
(217) Yan, Y. J.; Mukamel, S. *J. Chem. Phys.* **1991**, *94*, 997.

CR050165W